IDEA League

Master of Science in Applied Geophysics

Research Thesis

Forward modeling for electromagnetic subsea cable tracking

A better understanding of offshore wind turbine power cables

Sil Mossel

August 22, 2022

Forward modeling for electromagnetic subsea cable tracking

A better understanding of offshore wind turbine power cables

Master of Science Thesis

for the degree of Master of Science in Applied Geophysics at
Delft University of Technology
ETH Zürich
RWTH Aachen University
by

Sil Mossel

August 22, 2022

Department of Geoscience & Engineering · Delft University of Technology
Department of Earth Sciences · ETH Zürich
Faculty of Georesources and Material Engineering · RWTH Aachen University

Delft University of Technology

Printed in The Netherlands

IDEA LEAGUE
JOINT MASTER'S IN APPLIED GEOPHYSICS

Delft University of Technology, The Netherlands
ETH Zürich, Switzerland
RWTH Aachen, Germany

Dated: *August 22, 2022*

Supervisor(s):

Evert Slob

Tobias Stolz

Committee Members:

Evert Slob

Tobias Stolz

Florian Wellmann

Abstract

Failure of subsea wind turbine cables are the main cause for wind farm downtimes. Furthermore, 80% of insurance payouts to wind farms come from cable repairs and maintenance. Cable tracking is part of the wind farm cables maintenance scheme. Surveys are required for localisation and determining the depth of burial of the cables. Conventional surveying methods have shortcomings when it comes to localising offshore buried power cables, which can be resolved by using electromagnetic methods. From the measured magnetic field created by the cable, its position and burial depth can be inverted. Forward modelling the magnetic response of cables improves the understanding of their electromagnetic behaviour in one dimensional complex submarine environments. Maxwell's equations are the cornerstones of understanding the behaviour of electromagnetic fields, forming the basis of the models. Implementing numerical modelling packages like Empymod accommodate for boundary conditions in one-dimensional layered media to more accurately investigate the magnetic response of electric cables. Land measurements show that Empymod's numerical models can model cables in the accuracy range of 2-15% depending on the distance. New numerical model analyses show the influence of water depth, underlying layers, depth of burial, geometrical complexities and adjacent cables on the magnetic field. Surrounding resistivity contrasts together with changes in water depth change the measured magnitude of the magnetic field by up to 10%. Geometrical complexities have large effects on the magnetic field, sometimes completely changing the expected response. Therefore, twisted and irregularly shaped cables can pose problems when inverting for their position during surveys.

Acknowledgements

Firstly I want to thank everyone at League Geophysics for the great last half year. You guys made me feel welcome and part of the team! The weekly presentations also helped me learn a lot from everyone's work. Special thanks to the Seekable team, too! Tobias, Fiona and Michiel, you were always able to help me out whenever I had questions regarding coding, surveying and hardware. Big thanks to Prof. Evert Slob, for always being available, quick to respond to questions and just being very involved in my thesis. Lastly I want to thank Dieter Werthmüller, who was involved in the Empymod modelling part and helped me out just because he was interested.

Lastly, thanks to the Applied Geophysics students of 2020-2022! We had an awesome time in the Netherlands, Switzerland and Germany. I'll always remember our amazing skiing, hiking, climbing and relaxing trips, and of course working with you all. Even though Covid tried to make us lonely and miserable, you guys made it work for all of us! Hope to see you all very soon.

Delft University of Technology — Sil Mossel

August 22, 2022

Table of Contents

List of Figures

Chapter 1

Introduction

1-1 Context

The energy transition our world finds itself in is one of the greatest challenges of this generation. Sustainable energy generation, like on- and offshore wind power, is one of the most promising contributors in resolving this problem [Kitzing et al., 2020]. Acoustic and visual pollution make it more challenging to build the wind farms on land, increasing the demand in offshore wind farms [Bilgili et al., 2011]. Building wind farms offshore brings several extra challenges to the already complicated onshore projects. Cable infrastructure connects a network of wind turbines to substations, which can power the mainland. New developments in said cables increase the complexity, such as three-phase cables and higher power outputs, increasing the current [MacAskill and Mitchell, 2013]. Without this cable infrastructure working properly, wind farms either lose power in the energy transport, or they need to shut down temporarily for repair. 80% of insurance payouts to offshore wind farm projects come from cable damage [Dvorak, 2017], which means maintenance and repairs should happen effectively, efficiently and accurately. Consequently, it is vital that the buried submarine cable position can be comfortably acquired. When performing an offshore cable depth-of-burial (DoB) survey, it is imperative that cable tracking is understood well so it can be done most accurately and effectively. Multiple conventional cable tracking methods, like acoustic and visual methods, have issues arising from the fact that the cable is buried. Magnetic fields persist through the soil, however. The principle behind cable positioning using magnetic fluxgate sensors is to look at the changes in the magnetic field components between all sensor combinations, and then inverting for the position of the cable. Feeding accurate forward models into an inversion algorithm is faster than setting up cables or doing field measurements. Furthermore, forward models can explore the effects of varying field conditions in a controlled way, by adjusting only one or a couple parameters at a time. Therefore, the main question of this thesis is: How can forward models of the magnetic field of electric cables improve the efficiency and accuracy of detecting buried off shore wind farm cables to acquire their position?

1-1-1 An offshore wind farm grid

Offshore wind farm grids usually follow the same pattern: arrays of windmill cables run to a substation, which ups the power and sends it to the shore. On shore, the energy can be distributed over land. For larger distances high voltage direct current (HVDC) cables can be more efficient in terms of energy transmission, while HVAC cables cover shorter distances (up to about 60-80km) [Incore, 2019]. In Figure 1-1 a schematic overview of an offshore wind farm is shown. Different zones are highlighted in the aforementioned Figure, each locating a separate wind farm environment. The four areas can differ in several ways: subsurface layering, currents, cable geometry and water depths. The separate models discuss the changes in magnetic field due to the four sections and the associated likely varying parameters: the land area, the shoreface, the deeper offshore section and the 'busy' substation area.

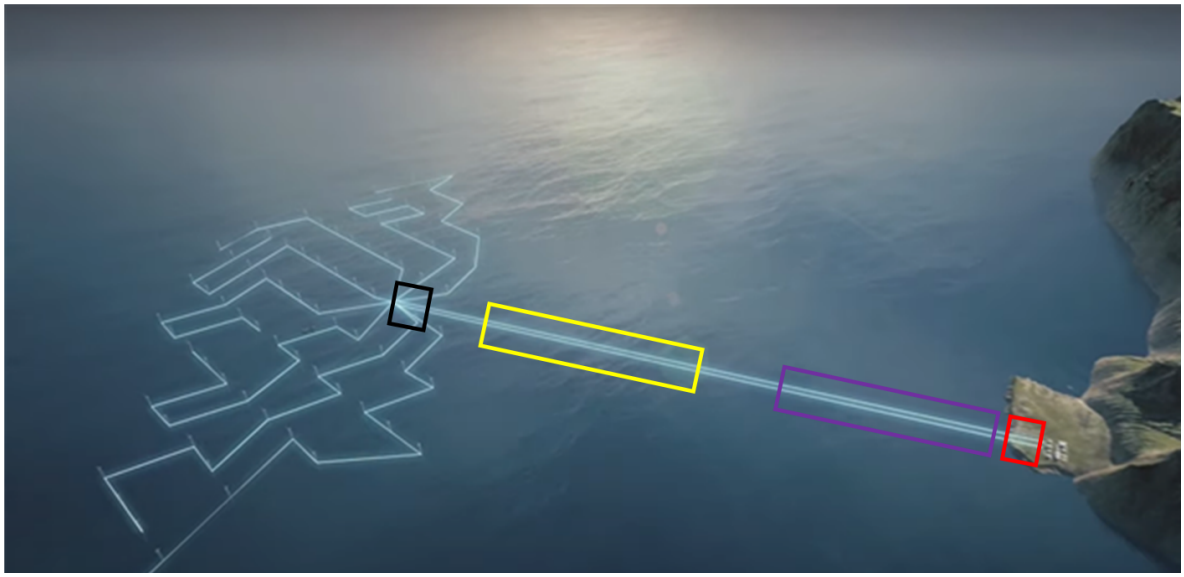

Figure 1-1: Overview of a wind farm separated in four sections: Substation and meeting point multiple cables (black), deep water with sifting sea environment (yellow), shallow upward slanting cable towards shore (purple) and landing cable (red). The same order can be applied from going left to right. Animation by [SiemensGamesa, 2022].

1-2 Problem overview

Cable tracking and maintenance using remotely operated vehicles (ROV's) or autonomous underwater vehicles (AUV's) are becoming more prevalent in industry. To reduce the high cost of insurance claims associated to cable damage [Dvorak, 2017], optimisation of tracking and repair is critical. The lack of GPS reception underwater, the varying sea currents and waves makes positioning of underwater vehicles troublesome [Littlefield et al., 2019]. AUV's though are looking more and more promising for cable inspection [Lubofsky, 2019], because there is no need for towing vessel and operator [Asif et al., 2006]. Two main methods exist for cable tracking: acoustic and visual methods.

1-2-1 Acoustic cable tracking

Acoustic tracking relies often on sonar methods and edge detection, which relies on looking at discontinuities in the brightness of the digital image, identifying (a)symmetries [Isaacs and Goroshin, 2010]. A Hough transform (in geophysics refered to as 'slant stack') is applied often, too. The peaks in this transform should correspond to line segments. However, other linear objects can also create peaks, which makes it not guaranteed that they correspond to cables, creating problems for AUV's doing surveys [Isaacs and Goroshin, 2010]. Several other acoustic methods exists. Subbottom profilers (SBP) are examples of shallow-penetration acoustics. These devices record 2D seismic lines, which makes tracking along a cable not practical. A large amount of crosslines are needed to accurately determine cable position and orientation. A solution was found which uses 3D volumes, the Pangeo Subbottom Imager (SBI). However, these SBI's are still very expensive and large, limiting their practical applicability, especially in shallow water [Dinn, 2012].

1-2-2 Visual cable tracking

Visual methods quite literally rely on sight. AUV's can recognise pipe and cable shapes and follow it in a straight line [Szyrowski et al., 2013]. Cables covered by underwater flora, a shifted seafloor [Wirth et al., 2008] or buried cables can pose problems for these methods, however. Luckily, magnetic fields persist through the subsurface soil [Gill et al., 2012]. Passive magnetic measuring methods can detect the magnetic field created by either a live windmill cable or one with an induced current [Xiang et al., 2016].

1-2-3 Measurement principle: fluxgate magnetometers

A wire carrying a current produces a magnetic field as a result of Ampère's law [Heald and Marion, 2012]. Figure 1-2 shows the direction of the measurable magnetic field B as a current I flows through a wire. This resulting magnetic field can be measured using magnetometers. Many different types of magnetometers, of which two are highlighted, exist, all having different benefits and downsides.

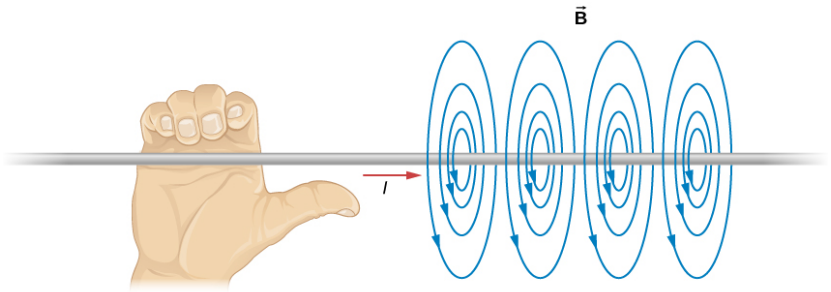

Figure 1-2: Ampère's law for the relation between the direction of flowing current and the resulting magnetic field [Moebs et al., 2016]

A fluxgate magnetometer is an instrument capable of measuring the strength of any component of the magnetic field, provided you have a three coils. A wire, whereto a current is applied, is wrapped around a ferromagnetic bar, which generates a magnetic field. Alternating the direction of the current creates a square sine, which cancel each others magnetic field other out. When an external magnetic field is present, the two directions are thrown out of balance, which allows measurements of the external field. By combining three fluxgate magnetometers, one in the X, Y and Z direction (or at least perpendicular to one another relative to a reference frame), every component of the magnetic field can be measured, which can be combined to acquire the total magnetic field vector. Using a bar is an inefficient geometry. When changing the bar to a square, the current drive coil can be wrapped around two sides of the square. Both sides will create the same magnetic field strength, with opposite directions, canceling each other out. A sensing coil can be wrapped around the full square, and the sensing soil will only be sensitive to the external magnetic field as the iron square goes in and out of saturation [Wei et al., 2021]. Again, three squares can be orthogonal to one another to acquire the total magnetic field vector.

Instead of measuring the vector components, some magnetometers measure the total magnetic field, or magnitude of the vector. Using the total magnetic field might be useful for determining distance to an object. For example, the magnetic field of a dipole decays with $1/R^3$, and that of a line with $1/R$ [Halliday et al., 2013]. Using the total magnetic field at two different locations can then help to determine the gradient, and therefore the distance to a magnetic object.

1-3 Numerical packages options

Four packages have been considered for the forward modeling of offshore cables: CUSTEM, SIMPEG, PETGEM and Empymod. All options share the advantage that they are open source Python packages, making them easy to access. Furthermore, they all have decent tutorials and documentation. The only reason to use different ones is their capabilities, shortcomings and processing speed. Firstly, CUSTEM is a package created for 3D finite-element modeling (FEM) (Figure 1-3) of controlled-source, transient, and natural-source electromagnetic data. For a detailed description of all the options, see [Rochlitz, 2022]. Tetrahedral finite elements based on weighted residuals and test functions make creating different total and secondary electric or magnetic field as well as gauged-potential approaches possible. The website of CUSTEM contains four modeling examples for frequency domain modeling, and three for time domain models. Furthermore, Rochlitz has produced two very comprehensible papers for both frequency and time-domain methods; [Rochlitz et al., 2019] and [Rochlitz et al., 2021], respectively.

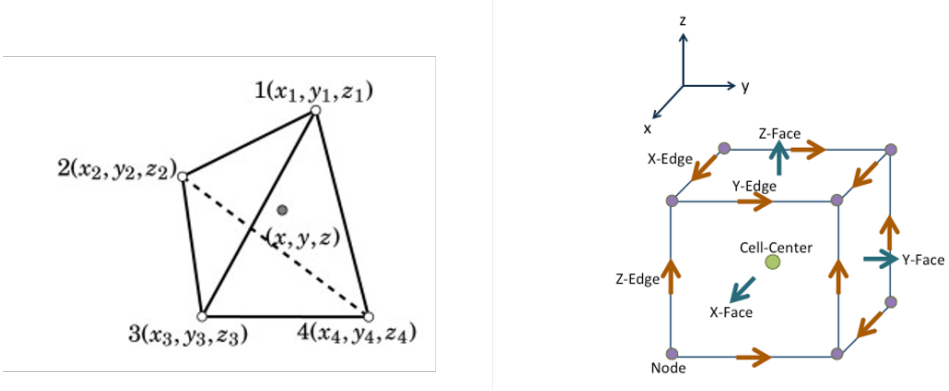

Figure 1-3: On the left a tetrahedral element for finite elements is shown, while on the right a finite volume cube is visualised.

SIMPEG uses finite volume method (FVM) for discretisation (Figure 1-3). For detailed descriptions, consider [Cockett et al., 2015]. Simpeg uses cubes, which provide less freedom in the scaling of volumes in a certain direction compared to FEM. However, when modeling straight cables, this actually is an advantage, since FVM requires less complex geometry construction. FVM discretises the fluxes on boundaries, and the numerical fluxes for this method are usually conservative and consistent [Eymard et al., 2010]. Therefore, FVM's are integrated often in fluid dynamic problems. However, [Hyman and Shashkov, 1999] shows that definitely FVM's are applicable for geophysical EM simulations.

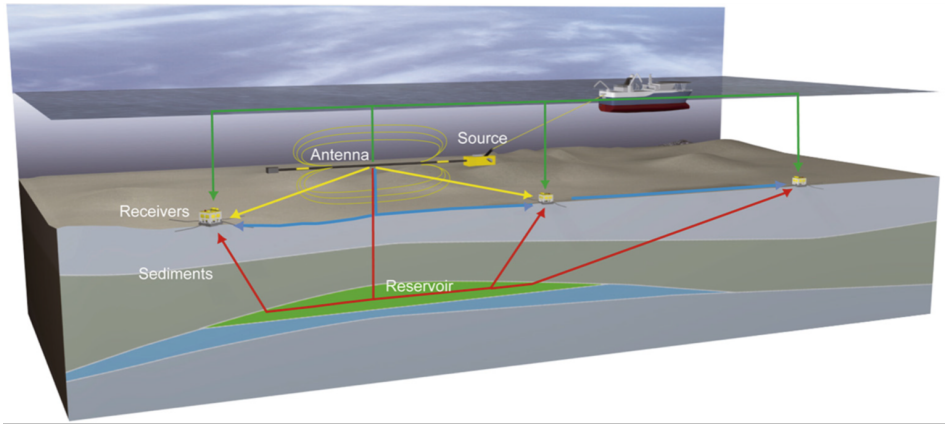

Figure 1-4: An example of a CSEM survey retrieved from [Castillo-Reyes et al., 2016]. Herein, a towed source with stationary receivers is used to map a resistive reservoir is more conductive surroundings.

PETGEM also uses tetrahedral finite elements. In this package, forward models are made for geological structures to evaluate their electromagnetic signature. PETGEM specialises in 3D Controlled-Source Electromagnetic method (CSEM, Figure 1-4) and 3D magnetotelluric (3D MT) modeling. For a detailed description of all possibilities, read [Castillo-Reyes, 2021].

Lastly, Empymod makes it possible to model three-dimensional electric or magnetic sources. These sources create electric and magnetic fields. In Empymod's 1D-layered Earth, there is vertical transverse isotropy (VTI) for resistivity, electric permitivity and magnetic permeability. Quote: "The computation is carried out in the wavenumber-frequency domain, and various Hankel- and Fourier-transform methods are included to transform the responses into the space-frequency and space-time domains." [Wertmüller, 2022]. The 3D electromagnetic field is produced from 1D layered media. The main reason for the development of this package is for CSEM, but it is flexible enough to model way different constructions and scenarios. The 1D layered case makes it laterally shift invariant, meaning very little geometry complexity is possible. However, this makes computations extremely fast. For the model generated in this thesis, it is assumed that the Earth can be considered a layered medium, and lateral variation are minimal. For this reason, it is fitting to use the most computationally efficient package, Empymod.

1-4 Outlook report

Literature shows limitations in the modus operandi of existing cable tracking methods, especially because of cable burial, e.g. [Szyrowski et al., 2013] [Littlefield et al., 2019] [Isaacs and Goroshin, 2010]. Electromagnetic cable tracking solves lots of these limitations, because induced magnetic fields and eddy currents persist through the soil into the seawater, where they can be measured actively or passively. The research in this master thesis is done to get a better understanding of the magnetic field behaviour used for cable tracking in the context of offshore windmill and energy grid cables by means of modeling and field measurements. The context of an offshore wind farm is divided up into four areas: the land, nearshore, offshore and so called busy zone. Theory about conventional cable trackers, magnetometers and physics related to magnetism form the backbone of the research of forward magnetic models. Analytical and numerical models are compared to on-shore measurements to get a good understanding of the possibilities and limitations of said models. Thereafter, hypothetical offshore measurements are generated using a package called Empymod, an open source Python package created for Controlled Source Electromagnetic Measurements and Modelling. However, this package is flexible enough to model wind turbine electrical line sources to get a better understanding of the influence of different parameters on the measured magnetic field signal. These parameters include: the influence of different layers in the subsurface below a cable which influence the TE and TM mode propagation [Slob, 2020], frequency and resistivity influence on attenuation [Heald and Marion, 2012], the effect of the water column depth, cables with varying geometries and near substation 'busy zones' for multiple cable interactions.

Chapter 2

Theory

2-1 Definitions

It is fair to describe Maxwell's equations in air as if they are in free space. Following [Slob, 2020], in free space, the wave propagation velocity c_0 and magnetic permeability μ_0 are exactly defined by equation 2-1a. Using these definitions, the electric permittivity ϵ_0 can also be exactly determined using equation 2-1b.

$$c_0 \stackrel{\text{def}}{=} 299792458[\text{m/s}], \qquad \mu_0 \stackrel{\text{def}}{=} 4 \times 10^{-7}[\text{H/m}], \tag{2-1a}$$

$$c_0 = \frac{1}{\sqrt{\epsilon_0 \mu_0}}, \qquad \varepsilon_0 = \frac{1}{\mu_0 c_0^2} \approx 8.854 \times 10^{-12}[\text{F/m}]. \tag{2-1b}$$

The space-time Maxwell's equations are given as

$$-\nabla \times \boldsymbol{H} + (\sigma + \varepsilon \partial_t)\, \boldsymbol{E} = -\boldsymbol{J}^e, \tag{2-2a}$$

$$\nabla \times \boldsymbol{E} + \mu \partial_t \boldsymbol{H} = -\boldsymbol{J}^m, \tag{2-2b}$$

wherein the material parameters are the electric conductivity σ (S/m), the electric permittivity in Faraday per metre (F/m) and the magnetic permeability (H/m). Unit "S" is Siemens, and determines the conductivity with SI unit S $= 1/\Omega$. Farad "F" describes charge at a certain current in a capacitor, describing the capacitance of a medium. Lastly, Henry "H" describes the inductance to relate the current to magnetic flux. The vectors in the right-hand sides of equations 2-2, are the source volume densities of electric current $\boldsymbol{J}^e$ and of magnetic current $\boldsymbol{J}^m$. Electromagnetic interference is assumed to be instant.

Often frequency domain formulations are considered, which can be obtained by taking a Laplace transform of a field, in this the electric field

$$\hat{\boldsymbol{H}}(\boldsymbol{x}, i\omega) = \int_{t=0}^{\infty} \exp(-i\omega t)\boldsymbol{H}(\boldsymbol{x}, t)\mathrm{d}t \tag{2-3}$$

With ω being the angular frequency $\omega = 2\pi f$. From this frequency transform, you can go back without losing information, such that you can map uniquely, forming a transform pair. For the Laplace frequency transform, this looks like.

$$\frac{1}{2\pi \mathrm{i}} \int_{i\omega=\omega_0-\mathrm{i}\infty}^{\omega_0+\mathrm{i}\infty} \exp(i\omega t)\hat{\boldsymbol{H}}(\boldsymbol{x}, i\omega)\mathrm{d}i\omega = \boldsymbol{H}(\boldsymbol{x}, t)H(t) \tag{2-4}$$

Since vertically transverse isotropic models are considered, the two-dimensional Fourier transform pair can be considered:

$$\tilde{\boldsymbol{H}}\left(\mathrm{i}\boldsymbol{k}_T, x_3, i\omega\right) = \int_{\boldsymbol{x}_T \in \mathbb{R}^2} \exp\left(\mathrm{i}\boldsymbol{k}_T \cdot \boldsymbol{x}_T\right) \hat{\boldsymbol{H}}(\boldsymbol{x}, i\omega)\mathrm{d}\boldsymbol{x}_T \tag{2-5}$$

and

$$\hat{\boldsymbol{H}}(\boldsymbol{x}, i\omega) = (2\pi)^{-2} \int_{\boldsymbol{k}_T \in \mathbb{R}^2} \exp\left(-\mathrm{i}\boldsymbol{k}_T \cdot \boldsymbol{x}_T\right) \tilde{\boldsymbol{H}}\left(\mathrm{i}\boldsymbol{k}_T, x_3, i\omega\right) \mathrm{d}V \tag{2-6}$$

2-2 Biot-Savart

"A static current solution for a finite line segment in free space can be acquired by combining Gauss' and Ampère's Law [Halliday et al., 2013]:"

$$\nabla \cdot \boldsymbol{B} = 0, \qquad \nabla \times \boldsymbol{E} = -\frac{\delta \boldsymbol{B}}{\delta t}, \tag{2-7a}$$

$$\oint_C \boldsymbol{B} \cdot d\boldsymbol{l} = \iint_S \epsilon\mu \frac{\partial \boldsymbol{E}}{\partial t} \cdot d\boldsymbol{i\omega} + \iint_S \mu \boldsymbol{J^e} \cdot d\boldsymbol{i\omega} \tag{2-7b}$$

B is the magnetic flux density, **E** is the electric field and the current density is **J**. The line integral is taken over a closed path C with line element $d\mathbf{l}$. C bounds surface S with surface element $d\mathbf{s}$. The divergence free property of the magnetic flux density means that magnetic charge does not exist. The bottom equation describes that a rotating magnetic field is created by a dynamic electric field and current, resulting in a static solution of the magnetic field [Ricketti, 2015]:

$$\boldsymbol{B}(\boldsymbol{x}, \boldsymbol{I}) = \frac{\mu_0 I}{4\pi} \oint_C \frac{d\boldsymbol{l} \times \boldsymbol{x}}{|\boldsymbol{x}|^3} \tag{2-8}$$

In equation 2-8, **x** is the distance vector, which describes the direction and distance between line segment $d\mathbf{l}$ at position **l** and the point of interest from where the field is calculated. For an infinite wire, equation 2-8 can be reduced to [Stratton, 2007]:

$$\boldsymbol{B}(\boldsymbol{x}, \boldsymbol{I}) = \frac{\mu_0 \boldsymbol{I}}{2\pi \boldsymbol{x}} \tag{2-9}$$

However, these solutions are static, and contain the magnetic field for all frequencies [Haus and Melcher, 1989]. When measuring a wind turbine cable, either a live one with a current of 50 Hz is measured, or a known signal is put on the cable. Therefore, the frequency component should be included in the solution for the magnetic field.

2-3 Whole-space solution

Starting with equation 2-10 from [Slob, 2020], the magnetic field $\hat{\boldsymbol{H}}$ is described in terms of Green's tensor and electric source $\hat{\boldsymbol{J}}^e$ by taking the dot product of the two, and integrating over the source position:

$$\hat{\boldsymbol{H}}(\boldsymbol{x}, \omega) = \int_{\boldsymbol{x}' \in \mathbb{D}^\omega} \left(\hat{\boldsymbol{G}}^{me} \left(\boldsymbol{x} - \boldsymbol{x}', \omega \right) \cdot \hat{\boldsymbol{J}}^e \left(\boldsymbol{x}', \omega \right) \right) \mathrm{d}^3 \boldsymbol{x}'. \tag{2-10}$$

Herein $\boldsymbol{x}$ and $\boldsymbol{x}'$ are the receiver and source position, respectively. Calculations will be done for $\hat{\boldsymbol{H}}$, even though it is not the measurable field. To acquire the measurable field $\mathbf{B}$, $\hat{\boldsymbol{H}}$ must be multiplied with μ, but this will be done later. The space frequency domain expression for the Green's tensor (equation 2-11) from an electric source to a magnetic receiver is the result of the curl of the scalar Green's function (equation 2-12):

$$\hat{\boldsymbol{G}}^{me}(\boldsymbol{x}, \omega) = \nabla \times \hat{G}(\boldsymbol{x}, \omega), \tag{2-11}$$

which has the source in the origin ($\mathbf{x}' = 0$) with scalar Green's function

$$\hat{G}(\boldsymbol{x}, \omega) = \frac{\exp(-\gamma |\boldsymbol{x}|)}{4\pi |\boldsymbol{x}|}. \tag{2-12}$$

For a line source in the x-direction, source term $\hat{\boldsymbol{J}}^e$ depends only on the current $\hat{I}(\omega)$ in that direction over the cross section of the cable, which is multiplied with impulse functions in the other directions

$$\hat{\boldsymbol{J}}^e = \hat{\boldsymbol{I}} \delta \left(y - y_{src} \right) \delta \left(z - z_{src} \right), \text{ with } \hat{\boldsymbol{I}} = \begin{bmatrix} \hat{I}(\omega) \\ 0 \\ 0 \end{bmatrix}. \tag{2-13}$$

Multiplying source $\hat{\boldsymbol{J}}^e$ with equation 2-11 results in

$$\boldsymbol{G}^{me}(x_{obs}, \omega) \hat{\boldsymbol{J}}^e = \begin{bmatrix} 0 \\ -\partial z \\ \partial y \end{bmatrix} \hat{G}(x, \omega) \hat{I}(\omega) \delta \left(y - y' \right) \delta \left(z - z' \right). \tag{2-14}$$

Combining this solution in the integral described by equation 2-10, and remembering that delta functions drop out when they get integrated, the result is

$$\hat{\boldsymbol{H}}(\boldsymbol{x},\omega) = \int \begin{bmatrix} 0 \\ -\partial z \\ \partial y \end{bmatrix} \hat{G}(\boldsymbol{x},\omega)\hat{I}(\omega)dx. \tag{2-15}$$

In the above equation, since the integral runs over all positions of x, only the Green's function depends on x, and the integral of the Green's function is the 0^{th} Bessel function over 2π: $K_0(\gamma r)/2\pi$, with [Heald and Marion, 2012]

$$\gamma = j\omega\sqrt{\varepsilon\mu - j\frac{\mu}{\omega\rho}} = \alpha + j\beta, \text{ and } \quad r = \sqrt{(y-y_{src})^2 + (z-z_{src})^2}. \tag{2-16}$$

Wherein the propagation constant γ is expressed in terms of the permittivity ϵ, magnetic permeability μ and resistivity ρ. Taking the derivative of the zeroth order Bessel function returns a Bessel function of the first order, and combined with the chain rule results in

$$\partial_y K_0(\gamma r) = -\gamma K_1(\gamma r)\partial_y r, \text{ with } \quad \partial_y r = \frac{y-y'}{\sqrt{(y-y')^2 + (z-z')^2}}, \tag{2-17}$$

with similar expressions for the partial z-derivative. Thereafter, the three components of the magnetic field $\hat{\boldsymbol{H}}(\boldsymbol{x},\omega)$ can be split up as follows:

$$\hat{H}_x(\boldsymbol{x},\omega) = 0, \tag{2-18a}$$

$$\hat{H}_y(\boldsymbol{x},\omega) = -\frac{(z-z')\gamma\hat{I}}{2\pi\sqrt{(y-y')^2 + (z-z')^2}}K_1(\gamma r), \tag{2-18b}$$

$$\hat{H}_z(\boldsymbol{x},\omega) = \frac{(y-y')\gamma\hat{I}}{2\pi\sqrt{(y-y')^2 + (z-z')^2}}K_1(\gamma r). \tag{2-18c}$$

To compare the above expression for the dynamic magnetic field to Biot-Savart's Law, the limit of γ should go to zero for a quasi-static solution [Haus and Melcher, 1989], which results in $\lim_{\gamma\to 0} K_1(\gamma r) = 1/\gamma r$ [Abramowitz and Stegun, 1972]. After dividing out γ, $\hat{\boldsymbol{H}}$ is only dependent on position. Thereafter, taking a source infinitely long on the x-axis, observed at position $(x_{obs}, y_{obs}, z_{obs})$ a distance r away from the source, and given $\boldsymbol{B} = \mu_0\boldsymbol{H}$, it can be concluded that

$$B_x = 0 \tag{2-19a}$$

$$B_y = \frac{(z_{obs} - z_{src})\mu I}{2\pi r^2} \tag{2-19b}$$

$$B_z = \frac{(y_{obs} - y_{src})\mu I}{2\pi r^2} \tag{2-19c}$$

Taking pythagoras to get the absolute value of the previously described components does indeed result in equation 2-9. In the non-static case (equation 18), the attenuation of the magnetic field depend mostly on the conductivity of the medium and the frequency used. Following [Heald and Marion, 2012], the aforementioned fields attenuate as

$$B = B_o \exp^{(j\omega t - \gamma z)} . \tag{2-20}$$

From these equations it is evident that when you have a medium with low resistivity, attenuation increases with increasing frequency. Furthermore, combining equations 2-16 and 2-1b, one can see that for a highly resistive medium (like air) the attenuation constant is close to zero. However, when considering the sea environment with conductive layer, γ could have an effect.

2-4 Reflection coefficients for half-space and layers

In CSEM measurements, one tries to determine the resistivity profile of the subsurface. An example is the depth of more conductive or resistive layers [Constable and Srnka, 2007]. Highly resistive layers have little attenuation, whereas conductive layers have more attenuation (see equation 2-16). On large scales the effects have been investigated. For example, when discussing diffusive EM field methods, [Slob, 2020] creates Figure 2-1 showing the different paths electromagnetic waves can travel when encountering abrupt resistivity changes. These different boundary conditions lead to different reflection and transmission coefficients and in the diffusive limit, lead to different field behaviour. The electromagnetic diffusive wavefield travels with the least attenuation per traveled distance through the most electrically resistive path.

The magnetic and electric fields can be decomposed in the transverse electric (TE) mode and the transverse magnetic (TM) mode. The former connects the vertical magnetic field to a particular mix of horizontal electric and magnetic components. It is transverse in the sense that there is only vertical isotropy, and the electric field is entirely perpendicular to the vertical axis. The TM mode is at a right angle to the TE mode, following Maxwell's equations. In this mode, the magnetic field is completely orthogonal to the vertical axis. Both modes together form the complete electromagnetic field. The TE and TM mode local reflection coefficients are described by [Slob, 2020]:

$$r_n^{TM} = \frac{\eta_{n+1}\Gamma_n - \eta_n\Gamma_{n+1}}{\eta_{n+1}\Gamma_n + \eta_n\Gamma_{n+1}} \tag{2-21a}$$

$$r_n^{TE} = \frac{\zeta_{n+1}\Gamma_n - \zeta_n\Gamma_{n+1}}{\zeta_{n+1}\Gamma_n + \zeta_n\Gamma_{n+1}} \tag{2-21b}$$

$$\Gamma = \sqrt{k_x^2 + k_y^2 - 4\omega^2/c^2} \tag{2-22a}$$

$$\eta = \sigma + i\omega\epsilon \tag{2-22b}$$

$$\zeta = i\omega\mu \tag{2-22c}$$

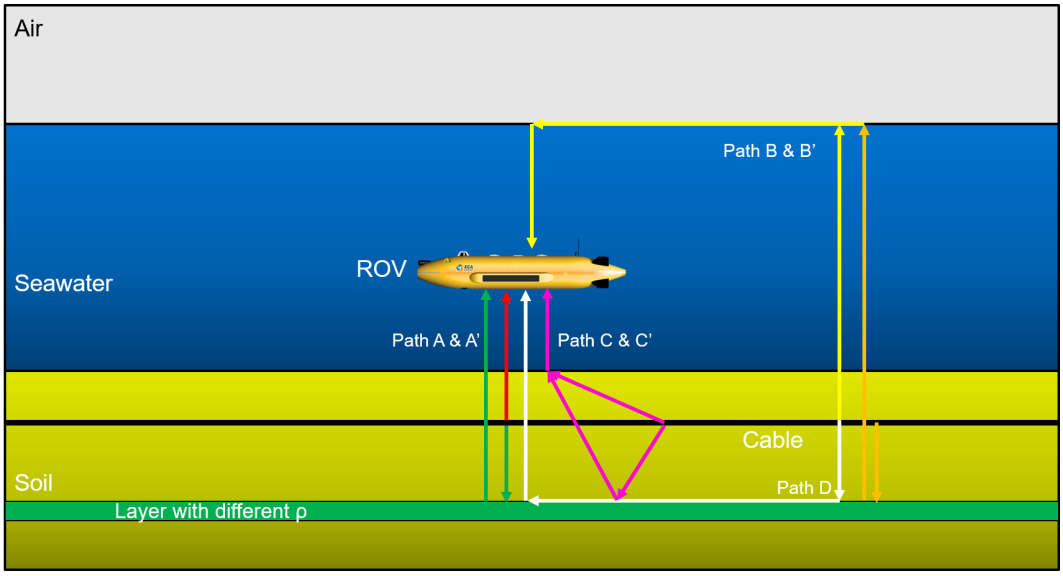

Figure 2-1: The main paths along which the electromagnetic waves travel in a layered medium to a survey device are indicated. Path A (red line) goes straight from the cable to the ROV with magnetometers. The air wave, path B (yellow line), goes straight up from the cable, travels along the sea-air boundary back down to the ROV. Path C (pink line) goes from the cable at an angle to the ROV and gets refracted in the seawater to the magnetometers. When the layer under the cable is very conductive, the reflection coefficient is approximately -1, the EM wave gets reflected and paths A' (green line), B' (orange line) and C' (pink line down-up-up) are possible. Lastly, when a layer is more resistive than the surroundings, path D (white line) is possible from the cable down, along the soil-layer boundary, up to the ROV. It is important to keep in mind that every path is possible at every point on the infinitely long wire and that these lines are just indications.

Γ is a term which contains the wavenumbers in the transverse directions (k_x and k_y), the frequency ω and the velocity c. In the diffusive approximation equations, η is only affected by conductivity $\sigma = 1/\rho$. The last term that needs to be defined is ζ, which is the product of the Laplace transform unit $i\omega$ and the magnetic permeability μ. Since the conductivity of air is zero, it means that in a half-space the local reflection coefficient $r^{TM} = 1$. At the same time, in r^{TE}, the ζ is similar in air as in any soil, making it possible to divide it out. The TE mode then returns $(\Gamma_n - \Gamma_{n+1})/(\Gamma_n + \Gamma_{n+1})$. The TE mode is complicated, and gives rise to the air wave depicted in Figure 2-1.

Chapter 3

Numerical tools: Empymod

Empymod whole and half space solutions are in principle analytical, just like Biot-Savart's law. However, layered earth models are only semi-analytical. Discretisation is required to approximate the sources. Space discretisation is often required in numerical methods. There are pro's and cons for both analytical and numerical solutions. On one hand, analytic solutions can usually not deal with complex geometries, heterogeneities, non-linearities and more realistic boundary conditions. These complex, more realistic conditions can be applied in most numerical approximations. However, numerical approximations are just that: approximations of reality. Approximations are usually necessary when dealing with real life problems, since the world around us is complex. Empymod approximates the Earth as consisting of only layers, taking vertical isotropy. Furthermore, the sources are approximations, too. At the boundaries the reflection coefficients as found in equations 2-21b and 2-21a have effect. As noted by Werthmüller, 2017, wavenumber calculations are based on Hunziker et al., 2015. The principle is based on computing the vertical electric field, and from that deriving the full 3D electromagnetic field in a VTI 1D layered mode [Hunziker et al., 2015]. Fourier and Hankel transforms are based on Key, 2009. It is useful to understand on a basic level the inputs and outputs on Empymod before going into detail with the different models. More detailed information can be found on the website, in the cited papers and in the Python package's documentation.

3-1 Different source types (dipoles, bipoles)

Empymod considers different source types, of which two are most accurate in approximating a line source: a sequence of dipoles and a finite length dipole, called a bipole. In CSEM, wire line sources are often approximated as dipoles because of the large distances involved [Streich and Becken, 2011]. However, when doing cable tracking the distances are way smaller, so the line shape is needed. If a sequence of dipoles is oriented in the way in which the current is flowing, granted the dipoles are sufficiently close together, a line source can be approximated, as seen in Figure 3-1. Note that in the figure the dipoles seem to have a finite size, but in the

model they are infinitesimally small. Furthermore, the closer you put the dipoles together, the better it approximates a line. In the calculations for the dipole sequence, every dipole-receiver pair is computed separately, making the process not super efficient. Moreover, it is key to remember that the distance dx needs to be multiplied with the solution to get a line source solution. Otherwise, when putting a lot of dipoles with a distance smaller than one metre, the solution blows up to infinity. Conversely, when the distance is larger than one metre, and the outputs do not get multiplied by dx, the modeled field will be too small.

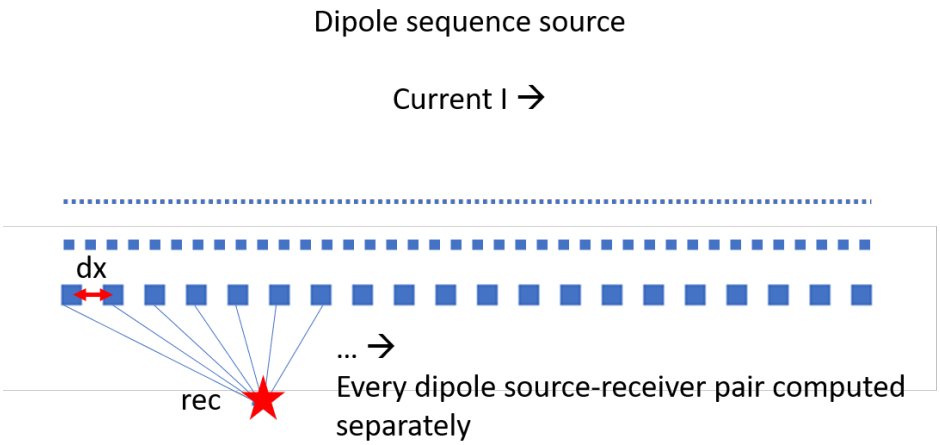

Figure 3-1: A sequence of dipoles approximates a line. The blue dots each correspond to an infinitesimally small dipole. The distance between two dipoles is dx. The blue thin lines from the dipoles to the receivers indicate that each dipole contribution is computed on its own.

These multiplication issues do not pose a problem in the bipole solution. The bipole solution uses a Gaussian-quadrature to apply weights to the source points and the receiver positions. More points means a better approximation, but also longer computations. Weights are given to each point, such that solutions do not blow up. Furthermore it makes sure that points that lie further contribute less. This process is faster than solving for every source-receiver position separately. Every receiver position still has to be computed on its own, though. More source points gives a better approximation, but in theory the Gaussian Quadrature makes it so that not a lot of points are needed. Figure 3-2 visualises the Gaussian distribution to compute the bipole source points contribution. It is clear that points further away are given lower weights.

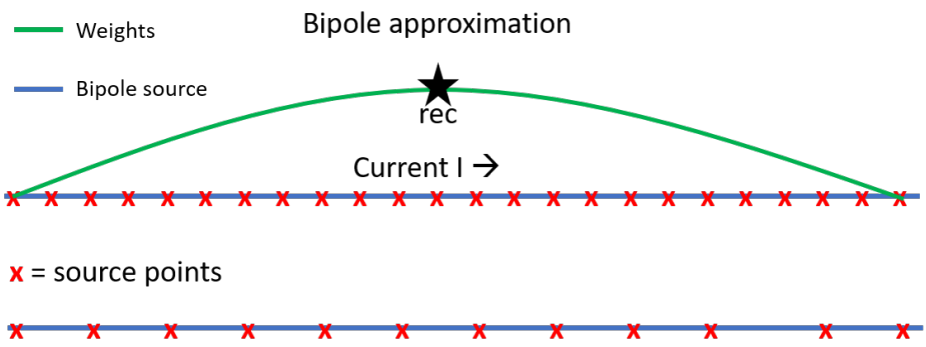

Figure 3-2: Bipole source visualisation. The red crosses represent the source points, which can be increased to better represent a line. An infinite number of source points should be a perfect line source. The blue line is the bipole source. The green curve represents the Gaussian weight distribution. Note that the end points of the source are almost not weighted at all, only slightly, whereas the middle point above which the receiver lies is weighted the most.

3-2 Inputs

The dipole and bipole both have different types of inputs considering their locations. Dipoles need the locations defined in (x,y,z) coordinates for every single point separately. In Empymod, it is not possible to put the dipoles at different depth levels, meaning you can only sequence them in one x-y-plane at a certain depth. The dipole receivers are similar. Since the dipoles diffuse equally in all directions, in the receiver the specific contribution can be investigated as seen in table 3-1. Selecting the correct source contribution-receiver direction pair then defines the direction of the current. Since in the coming models the source is considered to be electric, and only flowing in the x-direction, only the x direction's electric source contribution needs to be computed (column 1 of table 3-1). Thereafter, the corresponding magnetic field receiver for the x-magnetic field is 41, for the y-component 51 and for the z-component it is 61.

Input for source-receiver configuration dipoles		electric source			magnetic source		
		x	y	z	x	y	z
electric receiver	x	11	12	13	14	15	16
	y	21	22	23	24	25	26
	z	31	32	33	34	35	36
magnetic receiver	x	41	42	43	44	45	46
	y	51	52	53	54	55	56
	z	61	62	63	64	65	66

Table 3-1: The source-receiver combination input for dipole sources.

When creating bipole sources in Empymod, two points are selected between which the bipole is generated. These two points can have any (x,y,z) pairs. The source is then filled in with a certain number of source-points. For bipoles, the current is already in the direction between the two points. Thereafter, the desired component is output by inputting the appropriate receiver orientation. Empymod can use a left or right handed system, as visualised in Figure 3-3. Right handed systems are visualised in Chapter 5 for plotting purposes. Note that in right handed systems the elevation ϕ changes sign, where the azimuth θ does not.

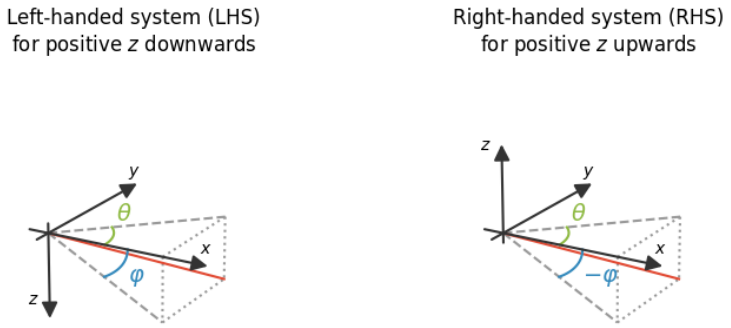

Figure 3-3: Two coordinate systems can be chosen: the positive z-axis down (left handed system) or up (right handed system).

Lastly, the depth resistivity model needs to be implemented. Figure 3-4 shows an overview of the inputs. The resistivity ρ, anisotropy λ, magnetic permeability μ and electric permittivity ϵ are all medium parameters that can be implemented in Empymod and are inputs for those layers. The layers exist between two boundary inputs. Therefore, the depth boundary input always contains one more value than the number of resistivity inputs.

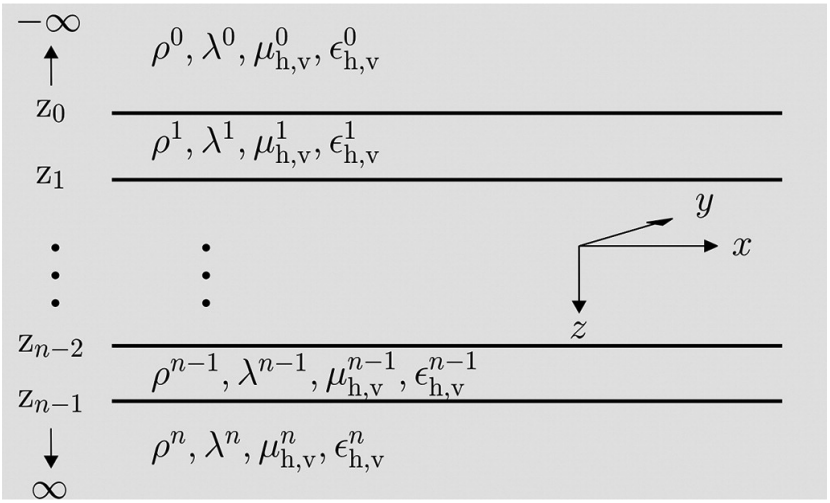

Figure 3-4: Resistivity model overview. The coordinate system here is left handed. Layers are given values regarding the resistivity, anisotropy, magnetic permeability and electric permittivity (ρ, λ, μ and ϵ respectively. Figure retrieved from Werthmüller, 2017.

Chapter 4

Field tests and numerical investigations

The setup of the models explore the behaviour of the magnetic field created by a wind turbine in different environments (see Figure 1-1). To help inform on the setup of the Empymod models, measurements were done on a land cable. In this environment and setup, the source strength, position, cable geometry, background noise and receiver positions could be carefully controlled or monitored. The Python package Empymod has two ways of approximating a cable: a sequence of dipoles, or a finite length dipole, or bipole. Both models are compared and should agree with the Biot-Savart's Law in a homogeneous whole-space with sufficiently low signal frequencies. Moreover, the dipole and bipole solutions are compared to one another, to see how many dipoles are needed to approximate a cable, and to see if both solutions agree. After the land data verification and other comparisons, the different wind farm areas are modeled. The cable runs from land, towards the beach and into the ocean. On the shoreface, water depth might influence the TE and TM modes of the electromagnetic signal. Offshore, the water depth is considered deep and constant. This area is the largest in terms of cable depth, and cables might experience geometrical effects like long bends. Furthermore, conductive and resistive layers in the offshore subsurface might influence the TE and TM modes, too. Finally, multiple cables come together near the substation, which can influence the signal of the desired cable which is being tracked.

4-1 Land scenario

From the offshore windfarm, the cables land from sea to be distributed to the users. Usually, these cable positions are fairly well known, which means they can be used to do tests on. Measurements were done on a self laid thin cable to verify the Empymod models. The data was recorded using fluxgate magnetometers (FGM's) for 100.000 nT, with an accuracy of 0.1 nT. Figure 4-1 shows the setup used with 5 FGM's in a vertical array. The idea of cable positioning using these sensors is to look at the changes in the magnetic field components

between all sensor combinations, and then inverting for the position for the cable. For more information regarding this inversion, consider Stolz, 2019. In this thesis, the modeled whole- and half-space solutions and measured effects are compared with regards to the total magnetic field and vector components, not to the position acquired using inversion.

Figure 4-1: The picture of the sensor array shows 5 fluxgate magnetometers in a vertical array, placed in light green holders. The FGM's alignment is measured by an inertial motion unit, or IMU, which is attatched to the pole. The sensor setup consists of a pole with sensors spaced 25 cm away from each other. The bottom sensor is located at a height of 0.5m, and the top sensor at 1.5m. The cables run to a white capture unit which pairs the information and sends it to a field laptop.

To compare the models to the measurements, two surveys were done, of which the layouts are in Figure 4-2. The first survey considered an open rectangular shape, seen as the yellow line in Figure 4-2. Measurements were done at distances between 1m and 15m in intervals of 1m. The cable was laid out in a square u-shape with the return path being the ground between the top right and left corner points. The long side was 40m long and the short vertexes 20m. Measurements were done by moving away perpendicularly from the long vertex. The signal had a frequency of 22.7Hz and a current of 33mA. Since a box signal current is only on half of the time, the average current is actually half of the peak current [Oppenheim et al., 1997].

The second set of measurements was done by moving away from a closed loop, which had the shape of a triangle (see Figure 4-2), with a resistor. A potential of 5V was put through the loop over a total resistance of 25 ohm, resulting in a 200 mA current. Due to the box car, this meant there was actually 100mA going through the cable. Again, every metre from 1 to 7 m a measurements was done to acquire the magnetic field components at different distances. The generator locations had the diesel power generator with the signal generator attached to it. They were as far away from the measurements as possible to reduce noise.

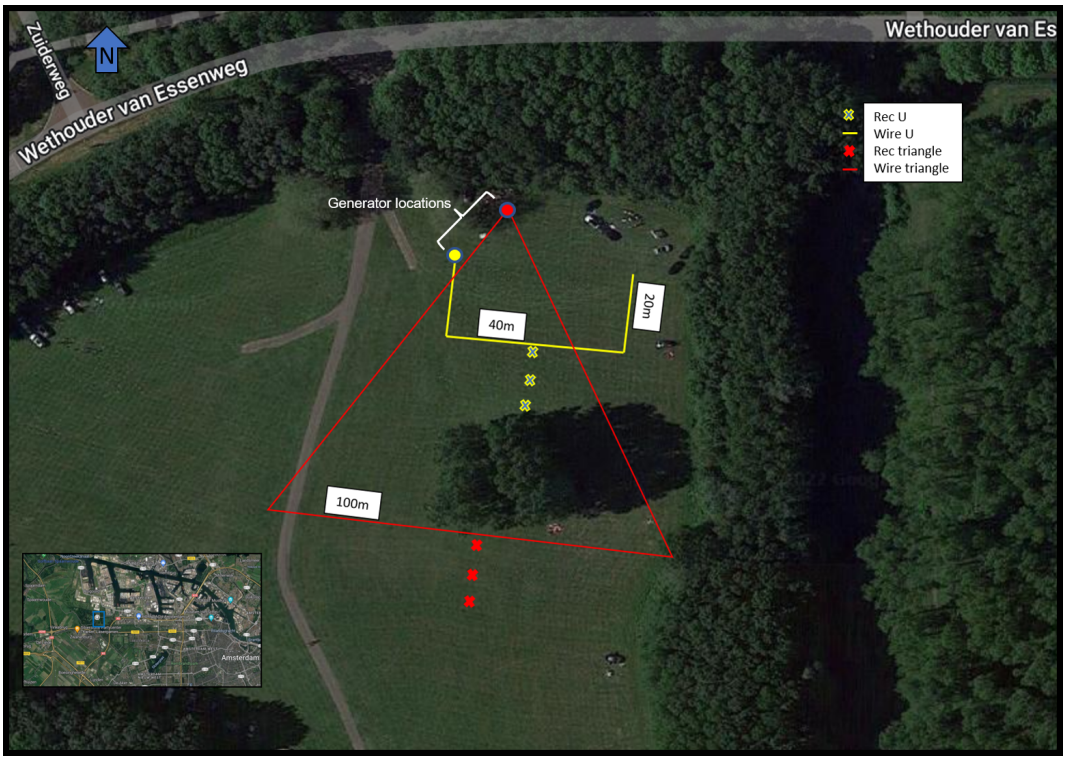

Figure 4-2: Satellite view of the measurement location and the layout. The x's give the approximate locations where the measurements were done to show that the sensors are moved perpendicularly away from the cable at 1 metre intervals, ensuring a known distance to the cable.

4-2 Attenuation

The aforementioned described layers (air, seawater and different soils) have dampened out fields according to equation 2-20. How much of the field attenuates was modeled in Empymod, again for the frequency response of the magnetic field generated by an electric current source. Two effects are explored: the distance dependency of the field at a certain frequency, and the frequency dependency of the field at a certain distance. The attenuated signal over distance at a specific frequency is interesting when considering a regular wind turbine cable. These cables have a set frequency of 50Hz [Garrido et al., 2003]. For the wind farm owners, surveying live windmill cables has an advantage over induced current or active measurements, due to the fact that the wind farm does not have to stop producing electricity. The disadvantage is that the survey cannot be done at a different frequency to reduce the influence on nearby

cables, which effects are explored later. The attenuation of the 50Hz frequency over distance is evaluated in Empymod from 3 to 30 metres distance. When passively measuring a cable, the signal frequency that is put into the cable is selected by the surveyor [Szyrowski et al., 2015]. Different frequencies are evaluated at a set distance of 5 metres to see the influence of the attenuation in distinct substances. The resistivity of seawater was set at 0.3Ωm, of the soil at 1.0Ωm and the air at 3×10^8Ωm [Cox, 1981]. The effect of attenuation is tested for three whole spaces (air, seawater and soil) and a layered case, as described by Figure 4-5. The geometry is similar as in the next model, and described in Figure 4-3. However, for the attenuation the source lengths are not altered, but only the frequency.

4-3 Comparison analytical solutions of line sources

Even though Empymod was developed for CSEM modeling, the diverse inputs make it also possible to investigate line sources at closer distances in the near field. Empymod can approximate a line source in two ways: a sequence of infinitesimally small dipoles, or a bipole (finite dipole), with a number of 'source points' which are the number of points for the Gauss-Seidel approximation. Chapter 3 describes in detail the implementation and meaning between the two source types. For this particular model, the sequence of dipoles and bipole solutions are compared. Since the Z-direction is the biggest component, only this direction of the magnetic field is evaluated for both source types in the frequency domain. A line of 100 metres long, located in the XY plane with constant depth Z = 0, is generated. The receivers create another XY plane from -200 to 100m in both X and Y, one metre above the source, to evaluate the vertical direction of the magnetic field. The model considers a whole-space of air, wherein the resistivity is set at $3 \times 10^8 \Omega m$. The orientation of the receivers is set at (elevation, azimuth) = (-90°, 90°) which is in the Z direction, meaning only the H_z field is evaluated. Empymod generates the H field, but B is measured. Since $B = \mu_0 H$, H should be multiplied with μ_0 to acquire B.

The simplest way to investigate the magnetic field of an electric current line source is by using Biot-Savart for an infinite wire, as described by equations 2-19a-2-19c. A comparison between the Biot-Savart solution and Empymod is made using the bipole function. When taking a *finite* length wire in Empymod, eventually Biot-Savart for an *infinite* length wire will not apply. The question is: at what receiver distance relative to the finite wire is Biot-Savart still decently applicable? A line is modeled in the xy-plane at 0 depth, running from 0 to 90 metres on the x-axis. Where the line runs in a whole-space is arbitrary because of the three dimensional shift invariance. However, to investigate the behaviour of the bipole at further distances, the line/bipole should be extended with more source points and for longer distances as to approximate an infinite wire. In the half-space solution, the influence of the TE and TM mode is investigated. As a starting point, the number source points of the bipole is set to 301, so one node at every 1/3 of a metre for the Gauss-Seidel integration/approximation. At a certain distance Empymod and Biot-Savart for an infinite wire will not agree. The relative difference can be compared to find an appropriately accurate receiver distance. To investigate the angle between the Biot-Savart and Empymod bipole solution, one needs the total field to produce the unit vectors of both solutions $\theta = cos^{-1}(\frac{\mathbf{a}\cdot\mathbf{b}}{|\mathbf{a}||\mathbf{b}|})$ [Stewart et al., 2020]. Herein, $\mathbf{a}$ is the Biot-Savart magnetic field vector and $\mathbf{b}$ is the Empymod vector, and θ the angle between them.

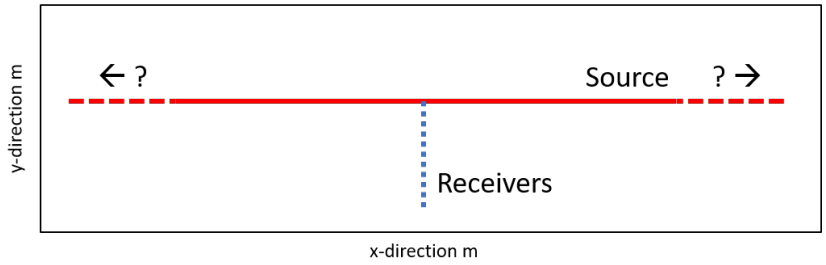

Figure 4-3: The geometry for Empymod and Biot-Savart's law comparison is shown here. Receivers are placed away from the source in a straight line to answer the question: at what receiver distance relative to the finite wire modeled in Empymod is Biot Savart still decently applicable?

4-4 Baseline parameters

After the land model verification, the frequency is set, the different sources are compared and the adequate source length to receiver distance ratio is determined, the subsea models can be generated. The baseline geometry for the models is as follows: an electric line source of 300 metres long is put 3 metres into the subsurface soil. This example depth is within the range of 0.6 to 7m described by cable laying companies Messe Düsseldorf and Hydro-International [Messe-Düsseldorf, 2018] [Gresty, 2019]. Fixed offshore windmills are limited to around 40-50 m water depth [Huera-Huarte, 2013], but shallower is preferred. Therefore, an arbitrary depth of 20m was chosen as water column, shallower than most wind parks, but 7 metres deeper than the shallowest part of the Doggerbank, where new wind farms are being developed [Johnston, 2017]. To model a cable tracker rover going over the cable, 5 receivers are moved over the source at an angle with 80 points. The receiver lines are about 45 metres long (44.72 metres from -20, -10 to 20, 10). The surveying angle is set at 30 degrees, to mimic an arbitrary survey. This angle will help to better understand the geometrical effects, as well as up and downgoing magnetic fields on either side of the cable. The baseline current is set at 106 Ampère. Figure 4-4 shows the geometry of the baseline receiver and source lines.

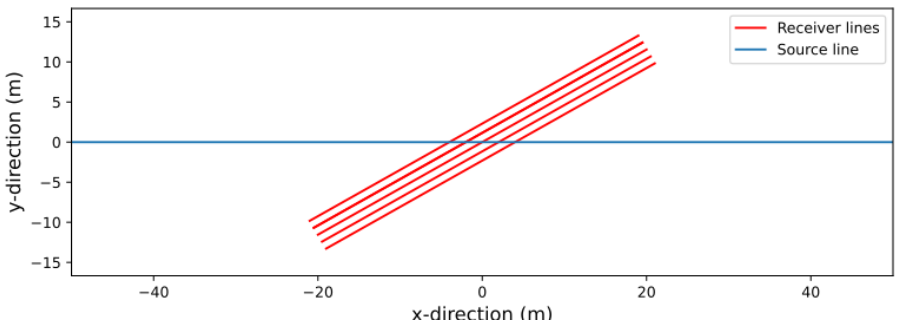

Figure 4-4: The receiver lines of the rovers over the source. Granted, the source actually extends from -150 to 150 m in the x-direction.

There are a couple of different layers with specific resistivities that have been picked to be tested in the models. Firstly, the seawater resistivity is set at 0.3Ωm, which is a resistivity often noted in research papers [Key, 2009]. Sandstone aquifers with salt water have resistivities evaluated in the range of 1-19Ωm [Singh et al., 2004]. However, since these models consider loose soil with seawater, the lower end of 1Ω is set for the baseline soil resistivity. The resistivity of air is so high (1.3×10^{16} to 3.3×10^{16}Ωm) that Empymod has trouble working with these numbers. However, when the resistivity is large enough, increasing it even more does not have an effect. Therefore, the air resistivity is set at 3×10^{8}Ωm. Further model inputs include the number of source points, which was found at around 1000 by trial and error, to ensure there are enough points to accurately approximate a line. A signal with 50 Hz frequency at a current of 106 Ampère was taken as to simulate a live windmill cable [Ferguson et al., 2012]. The output contains frequency domain response of the magnetic field generated by an electric source, which is what is contained in the results in the following chapter.

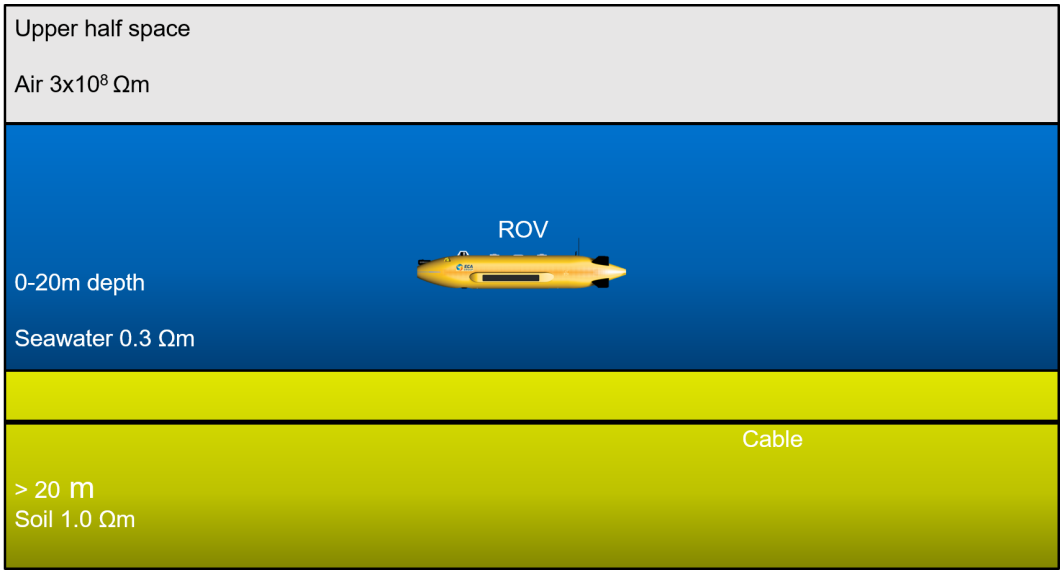

Figure 4-5: Baseline setup for the models. Not to scale. The resistivities of the appropriate layers are displayed in the Figure. The ROV will travel at a set depth along the seafloor. The cable in the baseline case is assumed straight at constant depth.

4-5 Varying water depth

Going from the backshore, to the foreshore, towards offshore, the water depth increases [Nichols, 2009]. Looking at equations 2-21b and 2-21a for the reflection coefficients combined with equation 2-16 for the attenuation, it is apparent that the water depth will influence the measured signal. Comparing the magnetic field vectors at different water levels can be modelled in Empymod to quantify the effects. Figure 4-6 visualises this model. It is important when comparing models to keep the rover at a constant angle to the cable. Furthermore, the distance should remain constant, such that only the water depth changes. The resistivities are the same ones as in the baseline case (Figure 4-5). The current is kept at a constant 106 Ampère to simulate a live windmill cable [Ferguson et al., 2012].

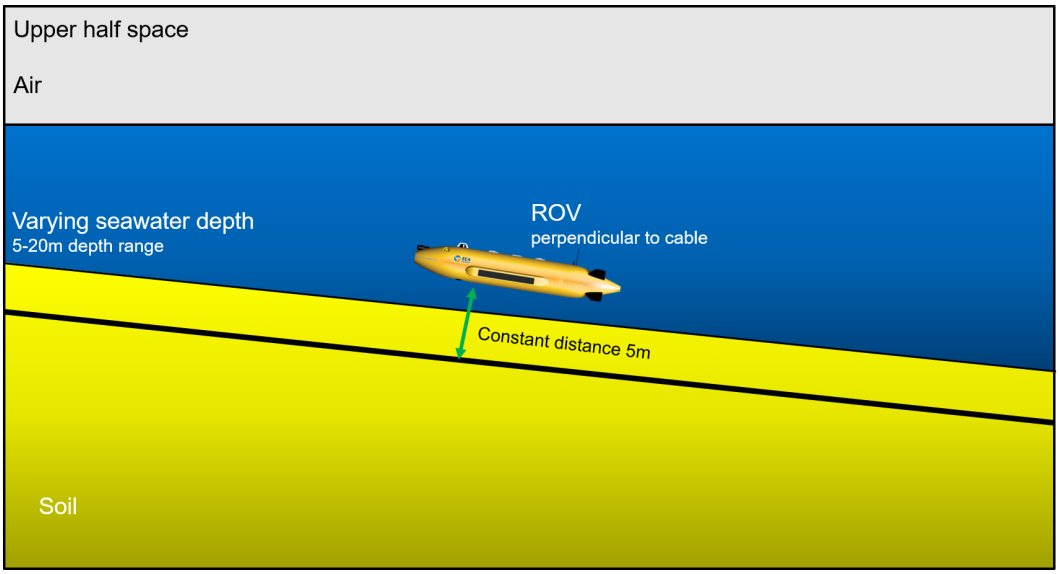

Figure 4-6: Shown is a scenario that could form when measuring a cable at the shoreface. Since the Empymod models are 1D, the model showed in the Figure cannot be generated. Therefore, multiple 1D models were made for water depths of 5, 10, 15 and 20 metres to see the changes in magnetic field with varying water depth. The measuring system was kept at a constant distance of 5 metres. The fluxgates were modeled to move over the cable again at an angle of 30 degrees, as per Figure 4-4.

4-6 Deeper water: geometrical effects, layers and a sifting seafloor

When cables are being laid, the ideal scenario places them in a straight line. Cable monitoring company PMI says that: "Perhaps one of the most common issues with subsea cables is their tendency to kink or bend. It is very easy to get a kink into the line when preparing to install cables and unkinking is a major exercise requiring special skills" [PMI, 2016]. Research is not clear about in what shape cables get kinked. However, in the Empymod package it is easiest to implement sinusoidal cable. Using the aforementioned x-ranges of the source and keeping the receiver positions the same, one can change the cable position in the second transverse y-direction to accommodate a sine. Figure 4-7 shows the geometry from a top view of this sine model. Two things are altered in these models: the amplitude and the period of the sine function. To accommodate for the sine, straight bipoles cannot be used. However, later will be explained that dipoles and bipole solutions are both sufficient to model a cable, so this poses no problem.

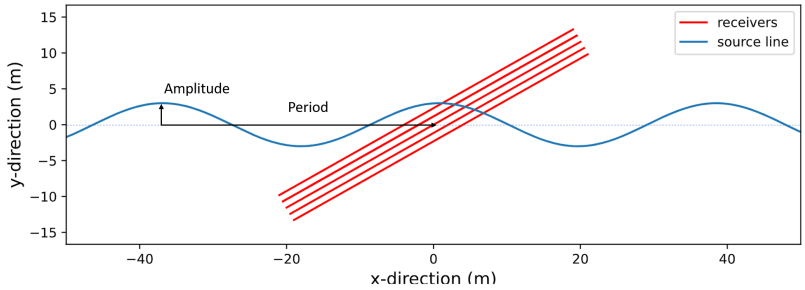

Figure 4-7: Top view of the sinusoidal geometrical effects models. The source is adjusted from the baseline case in that it now has the shape of a sine. The amplitude and the period can be adjust to view their effects on the measured magnetic field.

Furthermore, in this section different resistivity-depth combinations were tested to investigate their effects on the measured magnetic field. According to the TE and TM modes seen in equations 2-21b and 2-21a, layers of varying resistivity will influence the signal. It makes sense to test the effects of layers in this area, where it is possible that this is the only variation compared to a straight, steadily buried cable in constant water depth. It is important to note that Figure 4-8 looks as though there are 2D differences. However, this is not the case. For these models, layers were added in the subsurface at different depths below the cable with two possible resistivities: a high ($500\Omega m$) or a low one ($0.4\Omega m$), indicated in Figure 4-8 as red and green, respectively. Furthermore, the effects of a more resistive soil (3 Ωm) versus a conductive soil (0.4 Ωm) in these layered cases were considered. Therefore, 12 models were created.

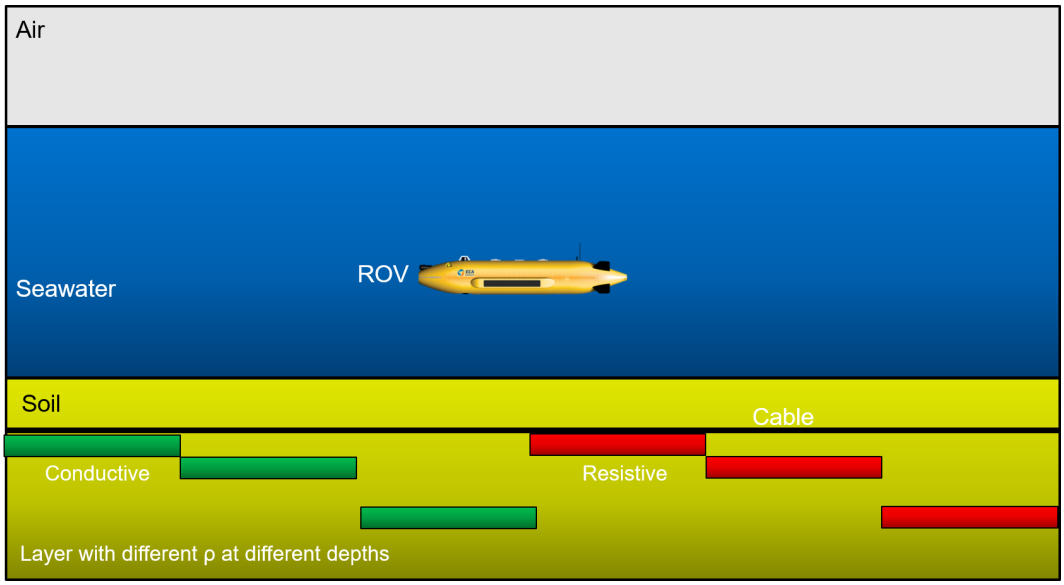

Figure 4-8: The resistivity layers models investigates layers at different depths. A resistive layer of 500Ωm was modeled at various depths, namely right below the cable, and 3 and 9 metres under it. The same was done with a conductive layer (0.4Ωm).

Lastly, offshore, the tides and waves can sift the seafloor environment [Nichols, 2009]. On top of a cable that was lain into a straight and even soil, sand ripples can build up. Furthermore, not all cables are buried at the same depth. Previously they were not buried at all, whereas nowadays they can be buried as deep as 5-7 metres [Messe-Düsseldorf, 2018]. Again, looking at the TM and TE modes, this topography or varying depth of burial can have effects on the magnetic field. 1D models of varying depth of burial can show the effects on the magnetic field of a sifting seafloor and depth of burial. Therefore, the model as depicted in Figure 4-9 was created in Empymod to study the effects. It is important to realise that Empymod generates 1D models, not 2/3D as visualised in the aforementioned Figure. Six models are generated with a depth of burial ranging from 5 to 0 metres deep into the soil. The distance from source to receiver is kept constant at 5 metres.

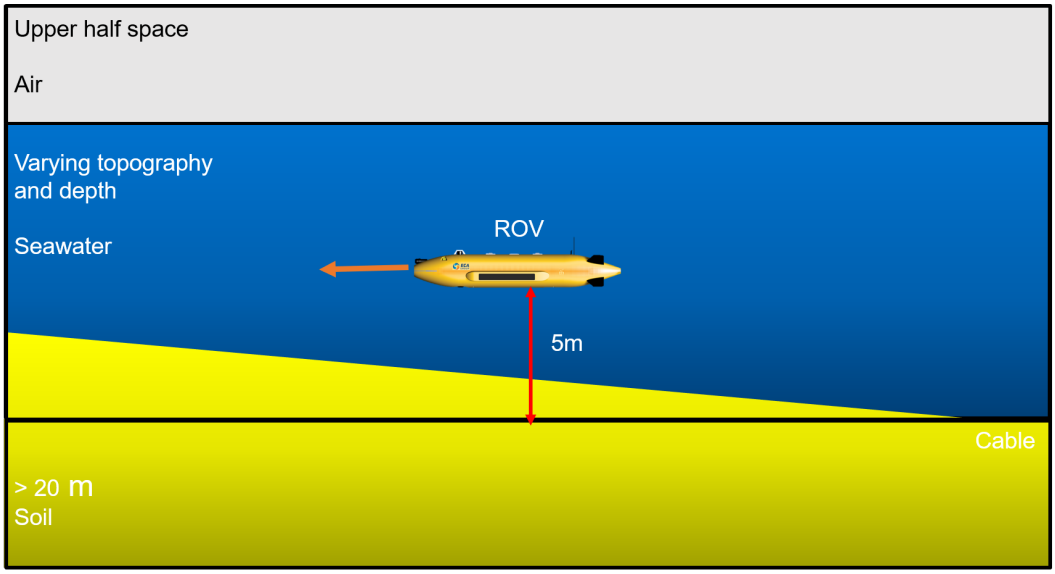

Figure 4-9: Burial depth conceptual model. 6 models are created to generate data for a cable burial depth of 5 to 0 metres. The ROV is at a constant 5 metres from the cable. Take note that the models are 1D, and not 2D as depicted here, so separate models are needed.

4-7 Wind farm inter-array

At substations multiple cables come together, and the power is increased for transportation to shore. When one wants to determine to locations of one specific cable, the cables next to it will influence the signal. It is easy to implement multiple sources in Empymod to see their effects. Wind turbine spacing ranges between 7-15 times the rotor diameters [JHU, 2011]. This range covers the common turbine spacing to an optimal one. With average rotor diameters of over 100 metres, this means that cables are over 700 to 1500 metres apart. Since magnetic fields decay with a factor of $1/R$, this effect is so small it is not useful to model it. However, cable interference is expected from the last column of turbines to the substation, where the cables come together at an angle. Figure 4-10 shows the geometry of this model setup. Cables are arranged as in Figure 4-10, and the sum is taken to determine the difference between a single cable and a cable with other ones around.

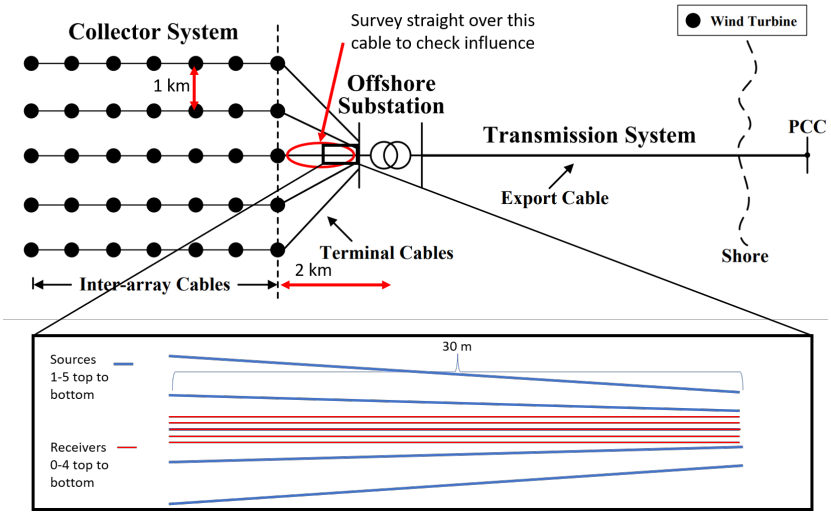

Figure 4-10: Busy zone overview as retrieved from [Moon et al., 2014]. The distance between wind turbines is set at 1 km. The distance from the last wind turbine to the substation at 2 km. The model will survey parallel the middle cable at a distance of 5 metres. The resistivity model is as explained in Figure 4-5 to measure the effects of the 4 adjacent cables next to it. The magnetic field components will be plotted in terms of amplitude for the rover path, which follows the receiver lines from left to right. Each receiver line represents one receiver moving with the rover.

Chapter 5

Results

In this chapter, models as described in the previous chapter are used to generate data. When comparing the data, the different magnetic field components can be displayed, as well as the total fields. Differences in angles between sensors or between solutions might also be useful to see how they change between the scenarios. The land scenarios compares the model to real measured land data. The results show that the Empymod package is adequate for modeling cables, provided the current and frequency are known. To determine an appropriate frequency, the attenuation is investigated for varying frequencies. However, for measuring live cables, the frequency is set at 50Hz. The results for the different sources in Empymod show which source type is better for which situation. Furthermore, the appropriate receiver distance to source length ratio is found when comparing the bipole to Biot-Savart's law. Thereafter, the hypothetical wind farm areas as described in Figure 1-1 are modeled. The different magnetic xyz-components, as well as the total fields are evaluated.

5-1 Land measurements

To validate the models, measurements were done on land in a controlled environment to be compared to the models. Figure 4-2 shows the geometrical setup, and Figure 4-1 the receiver sensor array. The measured data is compared to bipole sources. The geometry of measuring setup is 2D, so the sides of the cable could interfere with each other. This effect is however ignored. Both setups are modelled for two media: a whole space of air and a half space of air and soil. The dry soil resistivity was estimated at 2500 Ωm. However, considering equation 2-21a, the reflection coefficient of the TM mode will be -0.99 or -1 for all resistivities lower than $3\times10^6\Omega m$. Therefore, the ground resistivity is close to arbitrary, but within loose dry sandy soil ranges.

The triangle measurements are compared to a modeled wire and triangle in whole and in half spaces. The plots in Figure 5-1 show the y and z-components of the magnetic field for the 5 receivers for the modeled triangle. The receivers move away from the centre line at heights ranging from 0.5 to 1.5 metres. To reduce clutter in the Figures, for the other 3 plots only the middle sensor is plotted, so Figure 5-1 is easier to read. However, all sensors show the same behaviour. What is noticeable is that for the whole space, the three solutions match very well for the y-component. For the z-component, the measured data close to the triangle looks more like a modeled wire, and moving further away it looks more like the modeled triangle. For the half space, the z-component shows similar behaviour. However, the modeled y-component for both the modeled wire and triangle look less and less like the measured data when moving away from the source, with a difference of around 15-20%. The total fields are closely related to the z-component, especially when moving away from the cable. This makes sense, because moving far away from the cable the y-component goes to zero and the total field is the z-component. So, the measured total field close to the source corresponds better to the wire. Moving away from the source, the triangle model agrees better with the measured data, around the 2% accuracy mark.

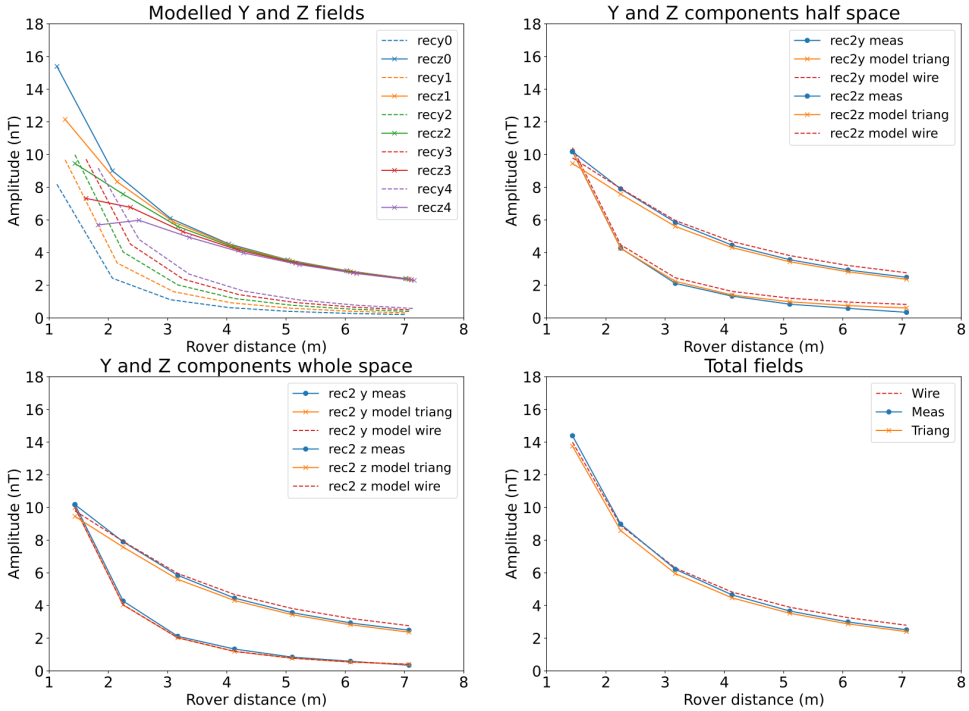

Figure 5-1: The plots show the measured data from the triangle compared to a modeled wire and a modeled triangle in whole and half space.

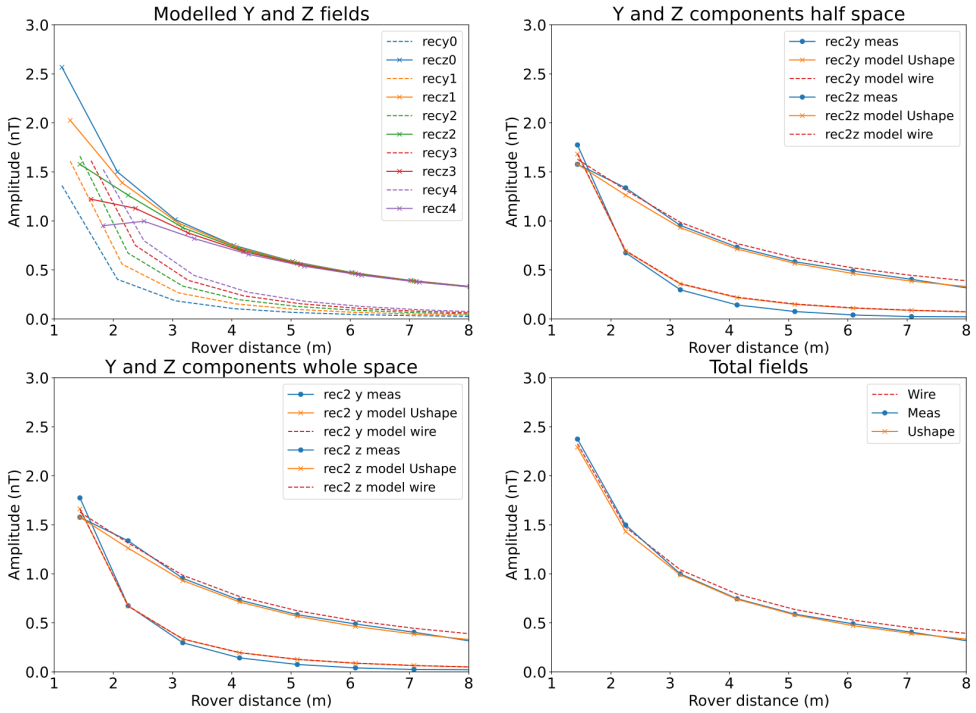

Figure 5-2: The plots show the measured data from the open square or u-shape compared to a modeled wire and a modeled u-shaped source.

The modeled magnetic field for the open square is compared to the measured data in the same manner as the triangle. The plots show the same type of data and components as described above. Also, the total fields are plotted for the whole space. There is a different behaviour of the field components between the measured data of the triangle and the open square. The y-components are measured lower than expected almost everywhere, except for closer to the source. The z-component, however, behaves similar as before: the measured data starts behaving like a line source, but further away more like an open square or u-shape. This observation is true for both the half and whole space. The total fields are related the same way as the z-components.

5-2 Attenuation

To select an adequate signal frequency for tracking cables, preferably the attenuation should be kept to a minimum. However, a lower frequency also means lower resolution, meaning there is a trade off. Resolution cannot be measured in Empymod, but attenuation can. According to equation 2-20, the magnetic field decays exponentially depending on the frequency and resistivity. Therefore, both parameters have effect on the measured signal, so both effects should be investigated. The aforementioned equation also shows that the resistivity and

frequency both have different influences on the real and imaginary-component of the magnetic field. The field can be expressed in terms of real and imaginary field, or in phase and amplitude. Figure 5-3 shows how these two representations are related.

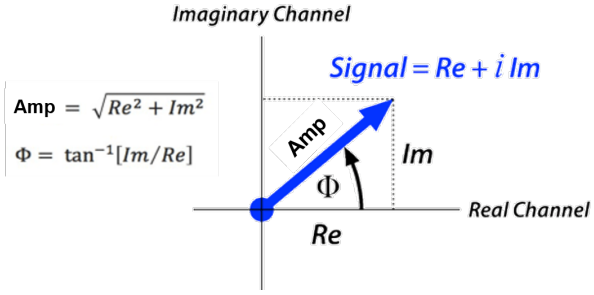

Figure 5-3: This figure relates the imaginary and real part to the phase and magnitude.

From Figure 5-4 it can be seen that indeed the frequency and resistivity have an influence, and that in separate media the two components react differently. The total magnetic field, however, does decay in a more predictable exponential fashion when increasing the frequency. Figure 5-4 shows the amplitude of the magnetic field related to frequency in sea air, soil and a layered case. The layered case consists of the baseline resistivity profile shown in Figure 4-5. The imaginary field increases and decreases again in every media but air. The turning point from increasing to decreasing imaginary field occurs at different frequencies in the separate media. For the layered case this is around 2000 Hz, for sea around 1250Hz and for the soil at 4000 Hz. In air the magnetic field is completely real.

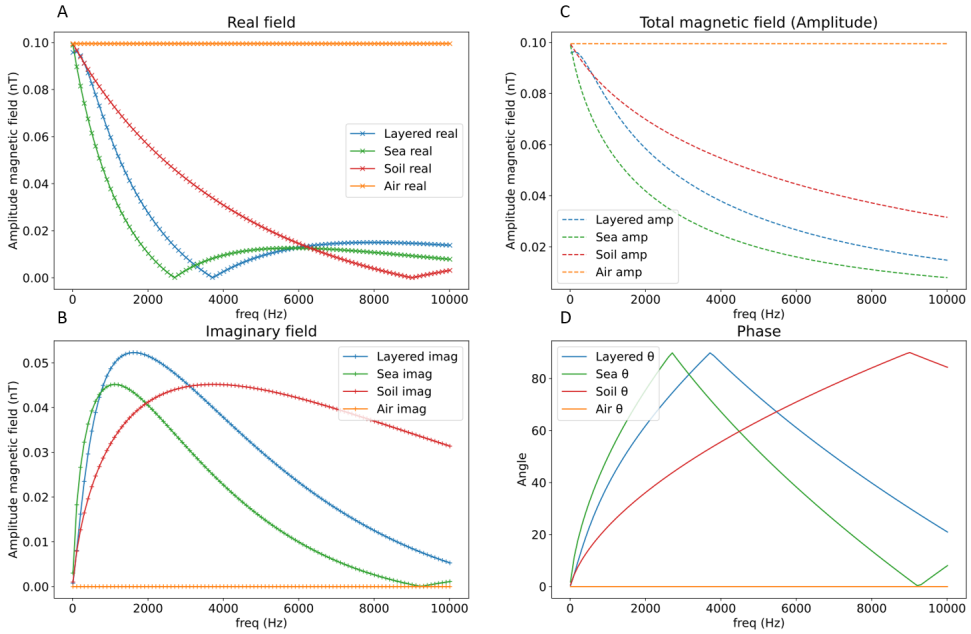

Figure 5-4: This Figure shows the different components for the magnetic field in varying media. Plot A shows the absolute value of the real part of the field related to the frequency. Plot B does the same for the imaginary part. Plot C describes the total magnetic field or amplitude and plot D the phase.

5-3 Model comparisons

5-3-1 Source comparison: dipoles vs. bipole

One can also approximate a line source by putting a sequence of dipoles between two points. To weight them, they should be multiplied with the distance between them. One can compare multiple parameters. In this example, the imaginary and real part and the relative error between the two solutions is evaluated in a depth slice between -100 and 200m in x and y. Most of the signal of the magnetic field is contained within the real part. Looking at Figure 5-4, this makes sense, since at 50 Hz the signal is almost completely real. At the end points of the line the error is the largest, but other than that, the solutions agree with each other, as seen in Figure 5-5. Especially when going further away from the cable the two solutions come more and more to an agreement. However, this can be attributed to the fact that the magnetic field goes to zero far away.

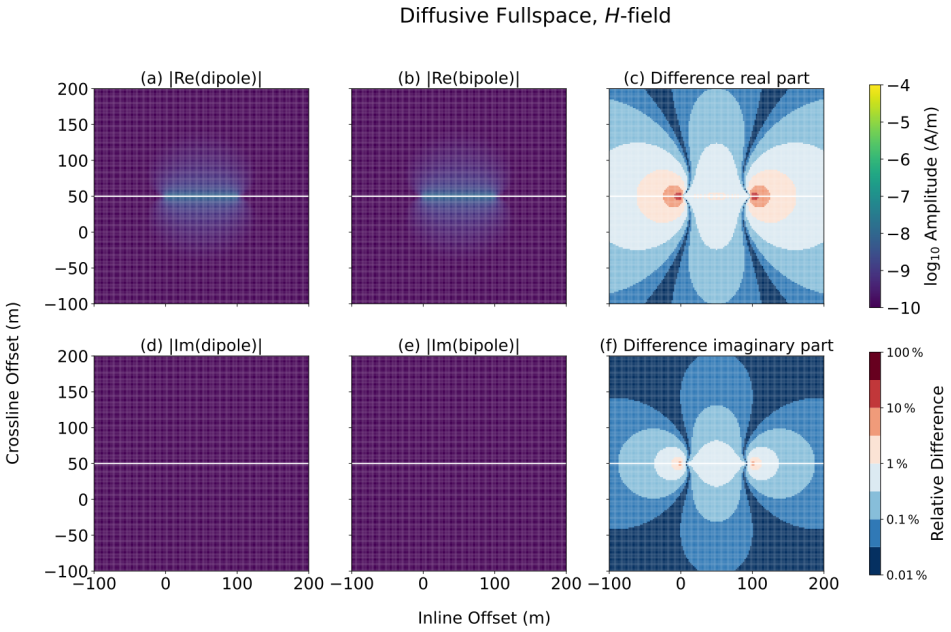

Figure 5-5: Bipole vs dipole comparison. On the left we see the results for the real and imaginary field for the dipole, and in the middle those of the bipole. The right-most plots show the relative error in the real and imaginary parts.

5-3-2 Empymod vs. Biot-Savart

To determine the validity of Empymod for approximating infinite line sources with a bipole, the bipole full and half space solutions are compared to the Biot-Savart's law. What is noticeable is that total magnetic field for the Biot-Savart and full space solution, as well as the Z field component from all three solutions, are close to identical. The biggest change is within the y-component in the half space solution. This change is related to the relative TE and TM modes. The Z field is determined by the TE mode and the Y to TM. Recalling the reflection coefficients from equations 2-21b and 2-21a, and setting the conductivity of air almost to zero, in a half-space the local reflection coefficient r^{TM} and r^{TE} are -1 and 0 respectively.

When taking a finite length wire, eventually Biot-Savart for an infinite length wire and the bipole solution will diverge. The question is: at what receiver distance relative to the finite wire, or source length, is Biot Savart still decently applicable? When testing this in Empymod and comparing Biot-Savart for an infinite line source to a finite length wire, it can be concluded that when the receiver is a 1/10th of the length of the wire away from its middle, Biot Savart and Empymod agree within 2%. For 1% accuracy between the two methods, the receiver distance should not extend more than 7% of the length of the wire. Therefore, to remain in the 1% accuracy range, the wind farm scenarios will have a receiver distance to source length ratio of 0.07, corresponding to 7%.

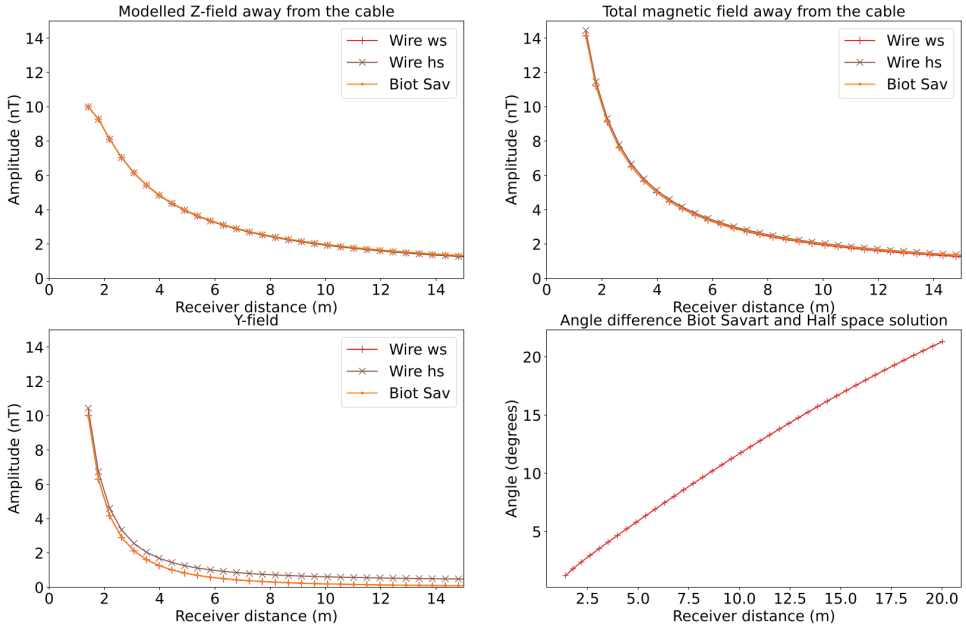

Figure 5-6: Biot Savart vs Empymod.bipole comparison. The total field, y- and z-components are compared for the Empymod whole- and half-space, and Biot-Savart solutions. The bottom right shows the angle difference between the vectors of the Biot-Savart and bipole half-space solution, which increases with increasing distance.

What can also be done is comparing the angle difference between two sensors at the same distance y moving away from a wire synchronously. This is exactly how the real life land scenario measurements were done, as seen in Figure 4-1. The inversion algorithm relies on the sensor angles, and the angle differences between all sensors to do intersection of lines afterwards to determine the cable location. When comparing these two angles from a set rover distance away from the wire, 3 different scenarios can again be related, namely the Biot-Savart and whole-space and half-space solutions in Empymod. What can be seen from Figure 5-7 is that the whole space and Biot-Savart solution have the exact same angle change between two sensors. This is notable, because as mentioned before, the magnitudes of the field components do not agree between these two methods after a certain distance. As expected, due to the TM mode effects of the half space solution, this angle difference differs from the other two solutions.

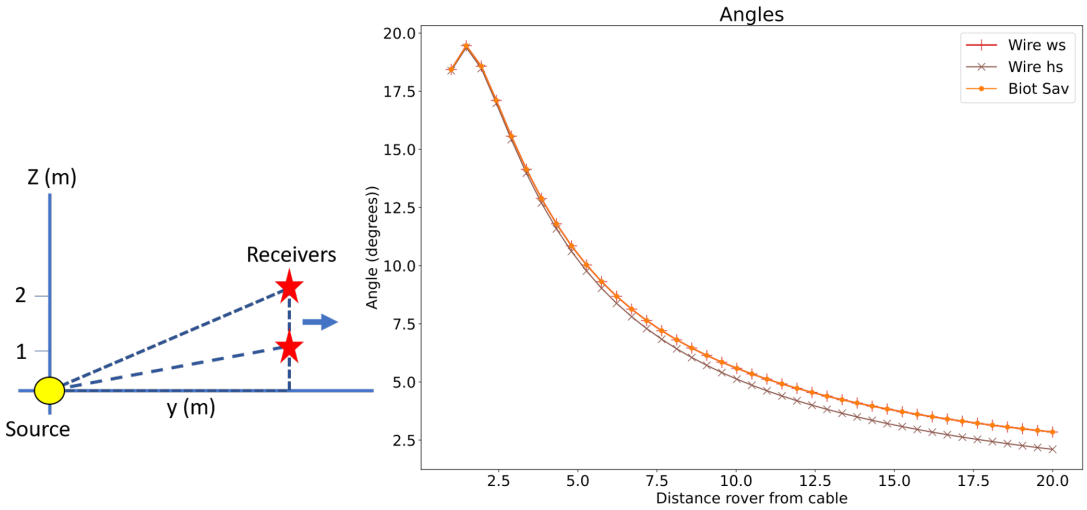

Figure 5-7: The difference in angle between a sensor placed at 1m height and one at 2m. The receivers are moving away in the y direction from the sensor, as seen on the left Figure. The right Figure shows the angle difference between Biot-Savart, bipole whole-space and bipole half-space solutions. It is obvious that the half-space diverges.

5-4 The baseline

The baseline conceptual model is visualised in Figure 4-5. This model is what most of the other models will be compared to. It is useful to see how a cable would react in a perfect environment, and thereafter see the changes. In Figure 5-8, just like in the other coming figures, the different components are plotted for the various sensors. The survey geometry is described in Figure 4-4, and the layers are visualised in Figure 4-5. When looking at the magnetic field response of the different components, most plots make sense. Sailing in the y-direction would mean you see a peak where the cable should be, around 0. Since the response is plotted against the rover path, the peaks of the y-field are not at the same time for every receiver. To see a response in the x-direction is unexpected, however. It is not exactly clear where this response comes from, but it might be an artifact of the numerical approximation of Empymod. In inversion, though, the effect is negligible, because it almost does not affect the angle of the fields compared to the y- and z-components.

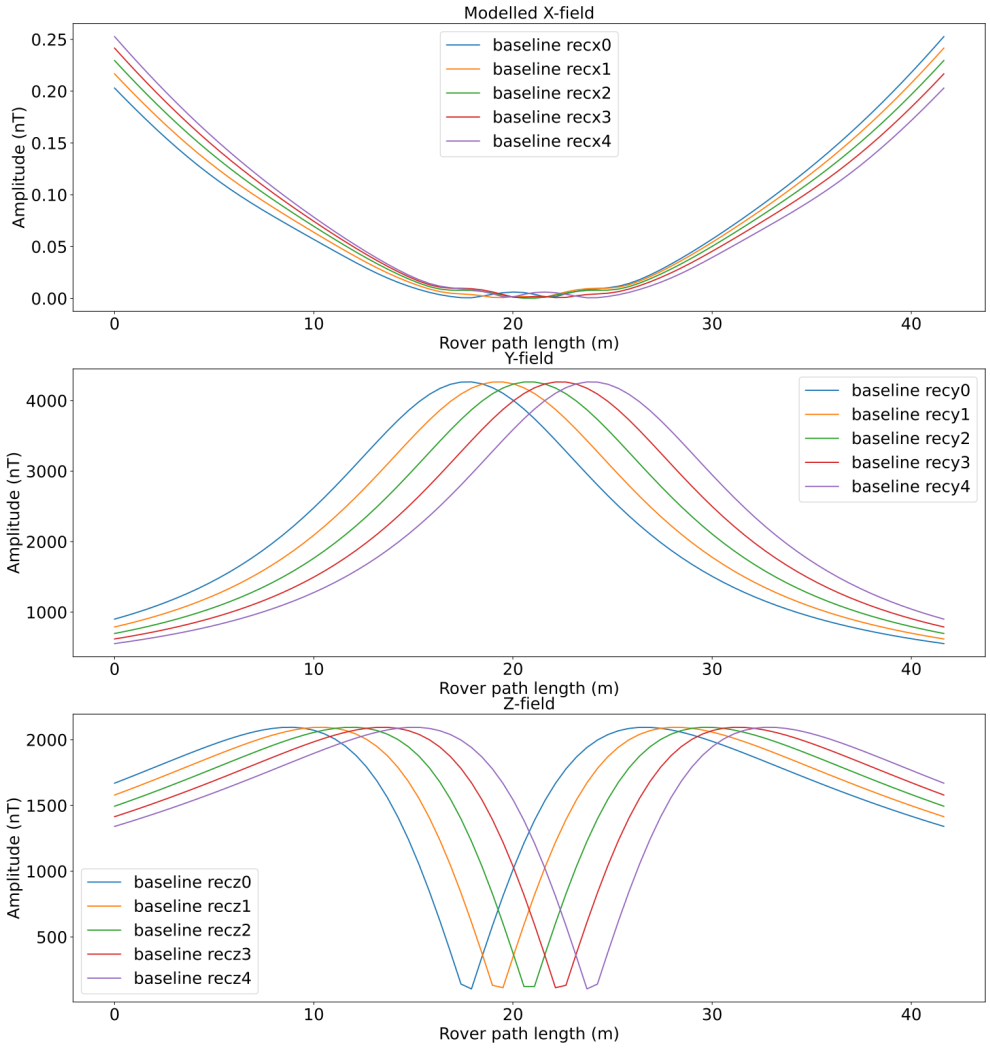

Figure 5-8: The baseline case sets the standard for the expected response of a live windmill cable when surveying the cable according to Figure 4-4. This Figure shows the separate x-, y- and z-components for all receivers when surveying over the rover's total path length. For the baseline case, since there are no particular artifacts, the responses for the receivers are identical, but shifted. This is because the receivers are offset from one another, as shown in Figure 4-4.

5-5 Foreshore

The TE and TM modes can change the values of certain components for varying water depth. Figure 5-9 shows the changes in components at different water depths. It is apparent that the z-component is not affected by the water depth, which makes sense from the definitions of the TE and TM mode reflection coefficients. Conversely, the y-component does change quite a bit, and increases with increasing water depth. Furthermore, the x- and z-component are zero above the cable, as expected from equations 2-19a and 2-19b. However, even though the x-component of the cable is small, it should be zero everywhere. Moreover, the x-field increases with decreasing water depth. It can be a numerical error of the Empymod package. Lastly, the y-component of the magnetic field decreases with decreasing water depth, almost in a constantly scaled fashion. The change can be attributed to the larger air wave associated with shallower water. The air wave has a different sign. The deeper the water, the more the air wave is attenuated according to equation 2-20, because the distance traveled is larger (see yellow path B in Figure 2-1).

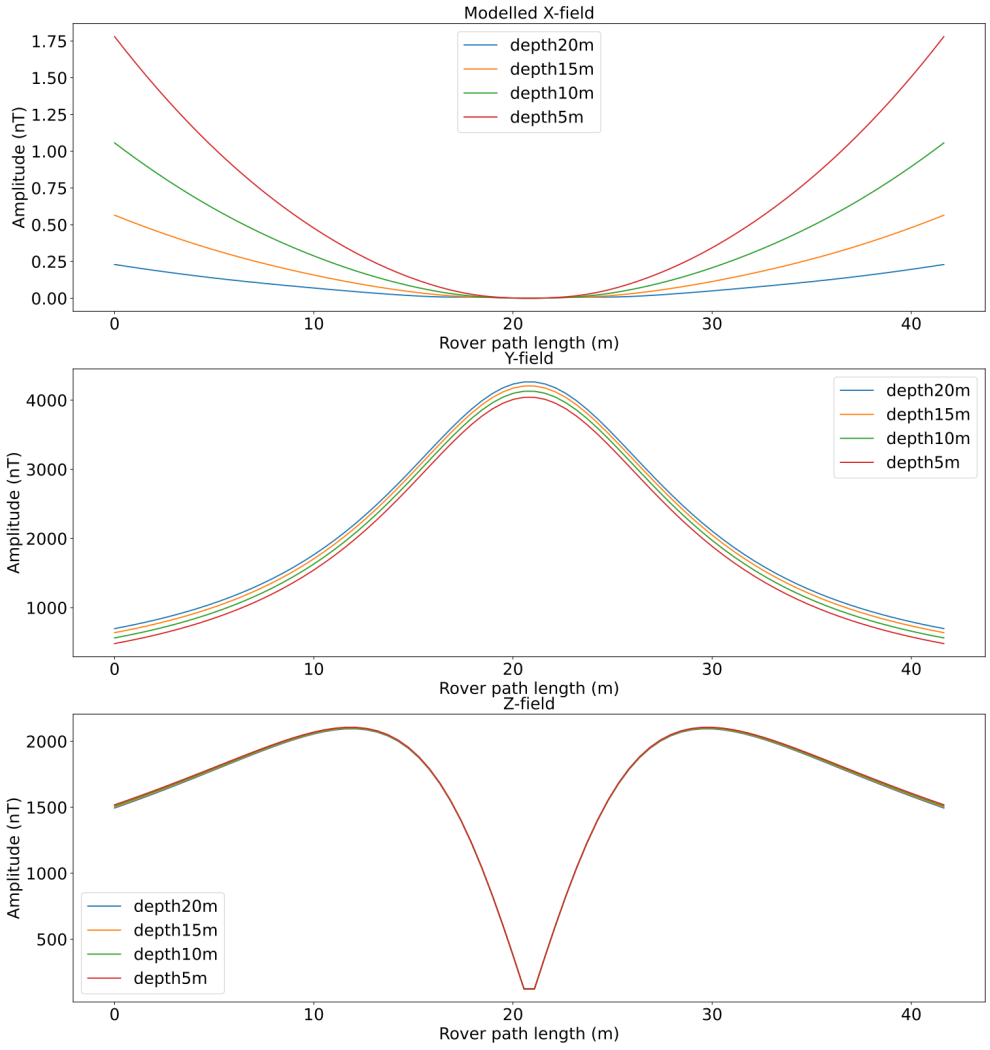

Figure 5-9: Magnetic field components for varying water depths. The results shown are of sensor 2, or the middle sensor in Figure 4-4. It is clear that the y-field is affected by the water depth, whereas the z-component is not. Furthermore the x-component is affected but this might be an Empymod issue. It will not have an effect on cable tracking.

5-6 Deeper water

5-6-1 Geometrical effects

The sine-scenario, visualised conceptually in Figure 4-7, compares 4 different models. The first modeled source is the baseline case, and is a straight cable. Thereafter, the model as depicted in Figure 4-7 is created. For the second sine source model, the source depicted in Figure 4-7 is altered and the amplitude is decreased by a factor 3 to create model 3. Thereafter, also the sine frequency is lowered or the period lengthened by a factor 2 to create the third and last sine. Figure 5-10 shows the resulting magnetic field components of receiver line 2 (see middle or third receiver line Figure 4-7). It is apparent that a change in amplitude has a larger effect than a similar change in the period. Additionally, it seems that a longer period emulates a straight line better when comparing the baseline case source 0 to sources 2 and 3. Source 3 has the longest period, and looks more like the baseline case in terms of y- and z-component for the magnetic field than source 2. This result is expected, because when the period is extended greatly, the sine source will practically be a straight wire. The y- and z-component do however closely relate all sources in some fashion, whereas the x-component completely changed. Since the baseline source lies in the x-direction, there is no magnetic field component. However, due to the sine the current direction changes, creating an x-component field. Granted, the x-component is still low compared to the y- and z-components of the magnetic field.

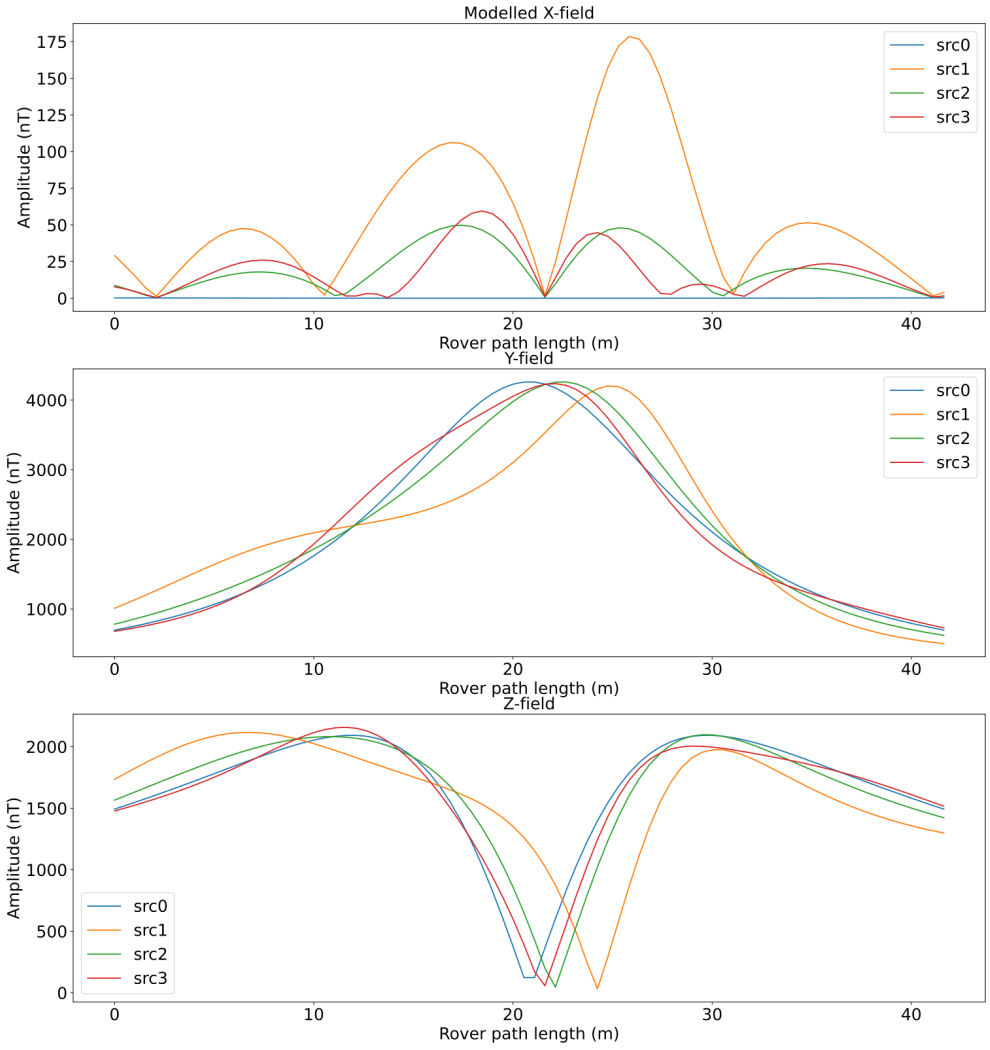

Figure 5-10: The magnetic x- y- and z-components for the different sine sources as described by Figure 4-7 and in the text above.

5-6-2 Layering

The possible depths and resistivities which are compared are found in table 5-1, from which 12 possible combinations can be made. In empymod, the bottom end of the layer is defined. For example: the first row of table 5-1 means that the upper half space is air with high resistivity, layer 2 extends from 0-20m depth with a resistivity of 0.3Ωm, corresponding to seawater [Key, 2009]. Thereafter, a 3 metre thick loose soil layer with low resistivity is added wherein the cable lies. Resistive or conductive layers are then added below this loose soil, whereafter the rest of the lower half space is filled with an arbitrarily resistive layer.

Scenario number	Resistivity (Ωm)	Depth of the bottom layer (m)
1	3e8, 0.3, 3, 500, 50	0, 20, 23, 26
2	3e8, 0.3, 3, 500, 50	0, 20, 26, 29
3	3e8, 0.3, 3, 500, 50	0, 20, 34, 37
4	3e8, 0.3, 3, 0.1, 50	0, 20, 23, 26
5	3e8, 0.3, 3, 0.1, 50	0, 20, 26, 29
6	3e8, 0.3, 3, 0.1, 50	0, 20, 34, 37
7	3e8, 0.3, 0.4, 500, 50	0, 20, 23, 26
8	3e8, 0.3, 0.4, 500, 50	0, 20, 26, 29
9	3e8, 0.3, 0.4, 500, 50	0, 20, 34, 37
10	3e8, 0.3, 0.4, 0.1, 50	0, 20, 23, 26
11	3e8, 0.3, 0.4, 0.1, 50	0, 20, 26, 29
12	3e8, 0.3, 0.4, 0.1, 50	0, 20, 34, 37

Table 5-1: Read the table as such: scenario 1 describes a resistivity of 3×10^8 Ωm above 0 metre, then between 0 and 20 metres depth there is a resistivity of 0.3 Ωm, between 20-23m a layer with 3 Ωm, then between 23-26m 500 Ωm and below 26 metres 50 Ωm. The first 6 scenarios are in a more resistive soil of 3 Ωm, and the other 6 in a more conductive one, at 0.4 Ωm.

Scenarios 1-3 have a resistive layer, where scenario 4 has a conductive one. What can be seen from Figure 5-11, is that the conductivity of the underlying layer has more effect than the depth variation of a layer with the same conductivity. The effects are only visible in the y-component, because the x-component should be zero. In Figure 5-12, scenarios 5 & 6 have a conductive layer, whereas 7 & 8 have a resistive one below the cable. Again, the conductive layer has the effect of reducing the y-component of the magnetic field due to the negative reflection coefficient of the TM mode, as described by equation 2-21a. Scenarios 9-12, as seen in Figure 5-13 say more about the depth, because the lines can be more easily distinguished. The order is 9 then 10 then 11 then 12 (blue orange green red) from top to bottom in the aforementioned figure. The deeper conductive in layer in scenario 12 has a larger negative effect on the magnetic y-component than the other layers. This is unexpected, since a deeper layer should have a more attenuated signal, which should result in a smaller change or larger field.

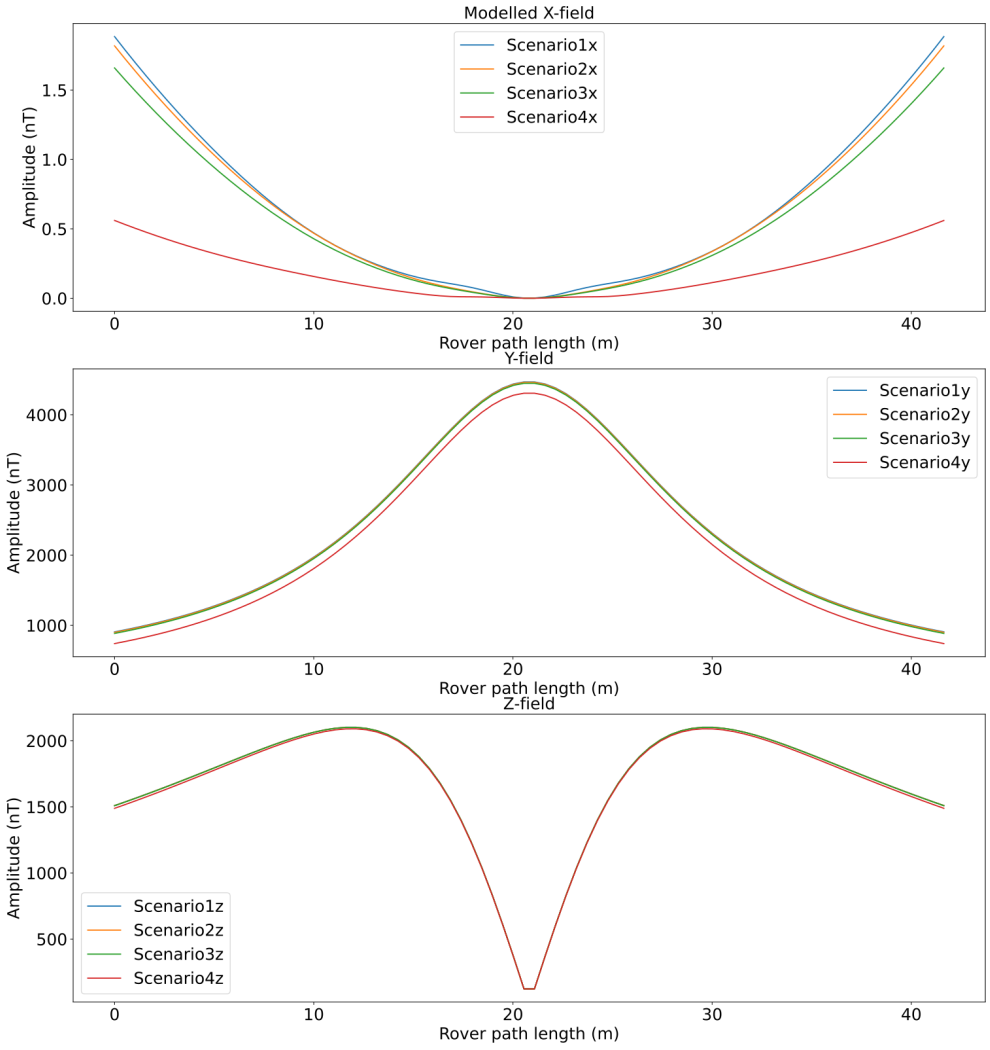

Figure 5-11: The magnetic x- y- and z-components for scenarios 1-4 as found in table 5-1 are plotted for the middle receiver (third) following the rover path as described in Figure 4-4.

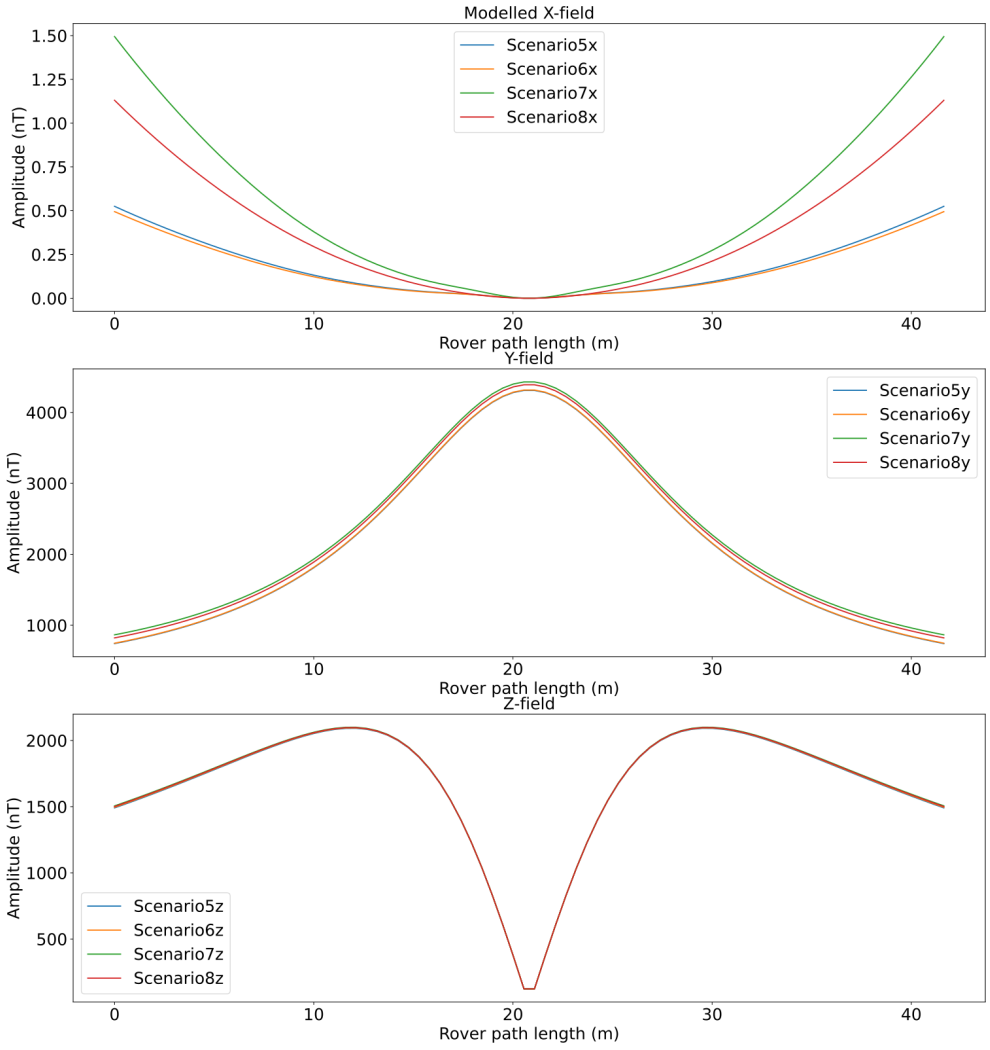

Figure 5-12: The magnetic x- y- and z-components for scenarios 5-8 as found in table 5-1 are plotted for the middle receiver (third) following the rover path as described in Figure 4-4.

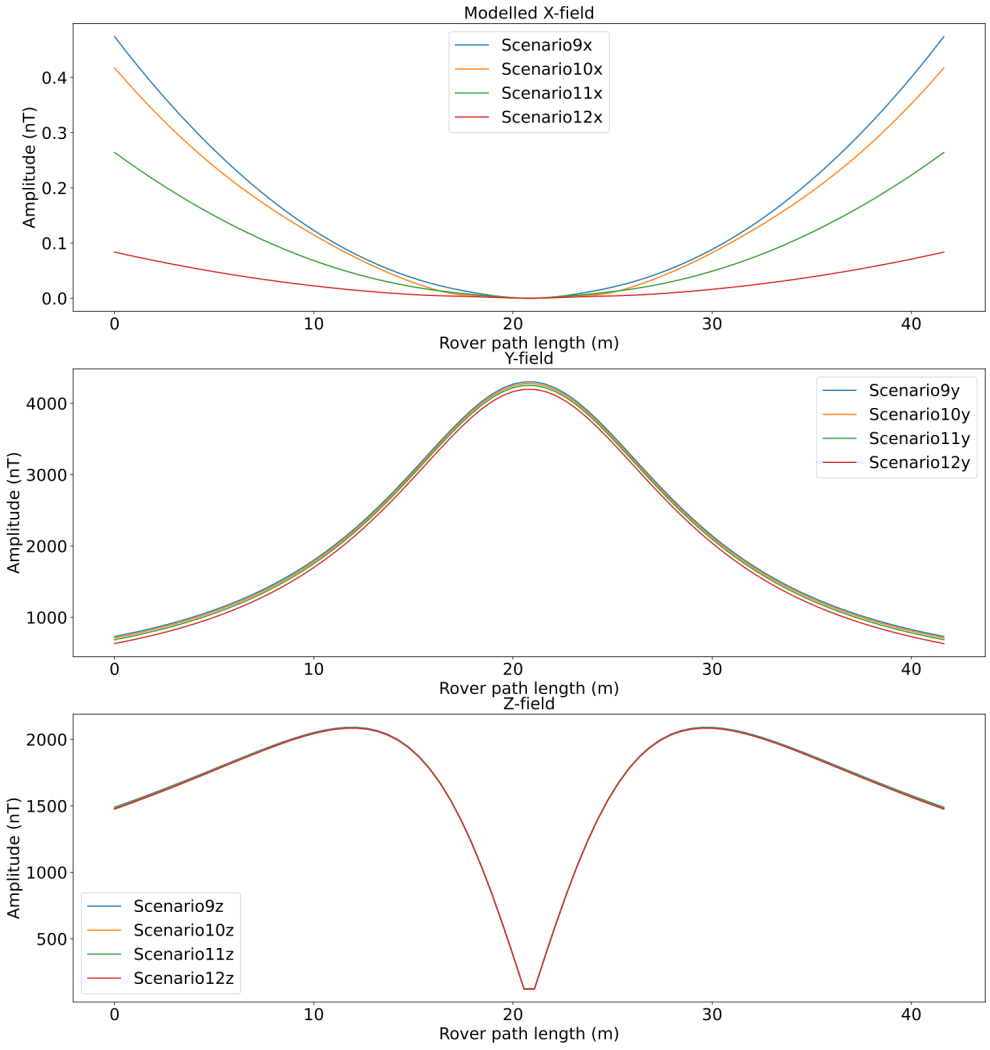

Figure 5-13: The magnetic x- y- and z-components for scenarios 9-12 as found in table 5-1 are plotted for the middle receiver (third) following the rover path as described in Figure 4-4.

5-6-3 Depth of burial

A sifting seafloor can have effects on the TM mode according to equation 2-21a. Figure 4-9 shows the conceptual idea of the model. The 5 models generate the magnetic field components for varying burial depths: from 5 to 0 metres. Figure 5-14 shows the results of the different components. It can be seen that the burial depth has close to no influence on the magnetic field of a buried cable.

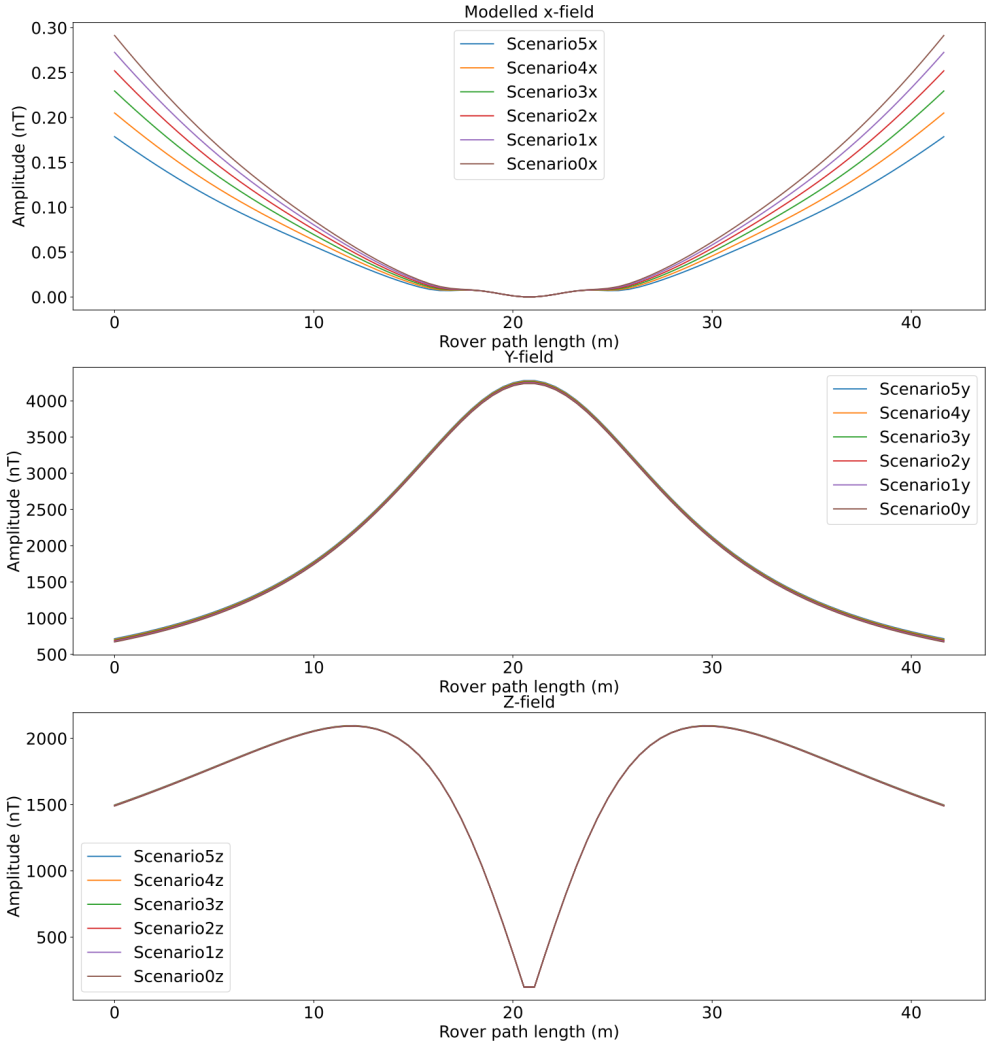

Figure 5-14: The magnetic field components for a cable with varying burial depth as seen in Figure 4-9 are displayed.

5-7 Interference in the busy zone

Cables coming together as described in Figure 4-10 might cause unexpected field behaviours. To check the difference to a single cable, the middle cable of Figure 4-10 is modelled of and shown in Figure 5-15. What is visible, is that the magnetic fields are constant as expected. However, towards the end of the cable, where the cable would reach the substation, some weird effects happen. Similar end effects are shown by the bipole-dipole comparison in Figure 5-5, meaning these end effects are consistent. Note that for the y-component, receivers 0 and 4 overlap, as well as 1 and 3, because the direction of the y-component is the same (minus) and the receivers are at the same distance form the source.

In Figure 5-16, the different components of the magnetic field are displayed for the busy zone with all five cables from Figure 4-10. As can be learnt from the right hand rule (Figure 1-2), some of the components will add up or be subtracted from each other. Numbering sources 1-5 from top to bottom in Figure 4-10, a table can be made for the expected influence on the different magnetic field components. Table 5-2 shows the contribution of all the sources on every magnetic field component.

Receiver # / component	x	y	z
0	-	-	+
1	-	-	+
2	0	-	0
3	+	-	-
4	+	-	-

Table 5-2: Expected result from the added sources when going from the baseline (one cable) to all five cables as described in Figure 4-10. The minus means a negative contribution and a plus sign means a positive contribution to that component of the magnetic field.

It is expected that for the middle receiver, which travels parallel over the cable, the x- and z-component cancel out and the y-component becomes the total field. However, for the receivers on either side of the centre cable, a different field is expected. Being closer to either of the sources means that the closer source will have more influence. Receivers 0 and 1 are expected to have a negative x-component which decreases when the cables come closer together. The z-field of said receivers should increase when the other cables come closer to the centre one. For receivers 3 and 4 it is the other way around: the x-component of the magnetic field starts out positive and will increase, whereas the z-component will start positive and decrease over the survey. Both the x- and z-component of the magnetic field for all receivers show expected behaviour. The y-component should decrease more and more as the cables come closer together.

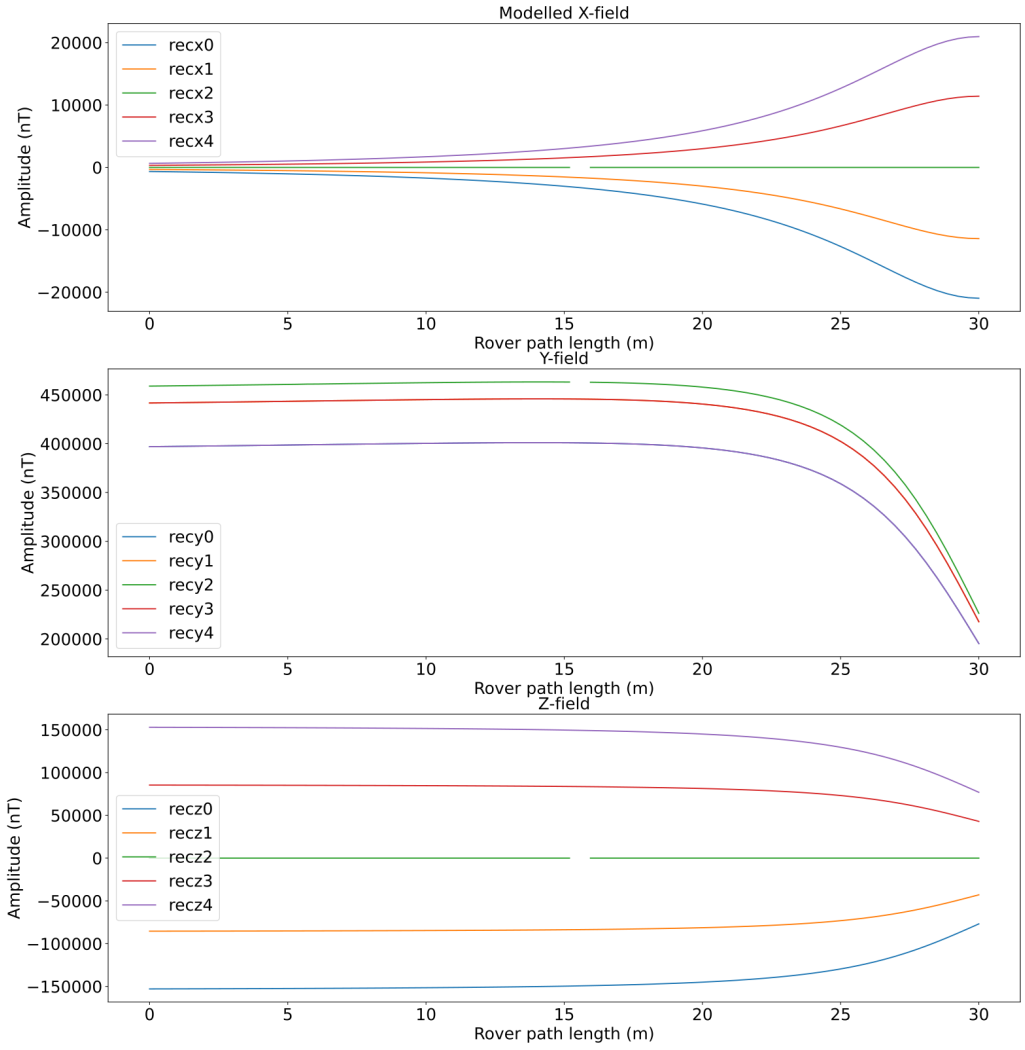

Figure 5-15: The magnetic x- y- and z-components for the substation busy zone area are presented as conceptualised in Figure 4-10. Note that only the middle cable from 4-10 is modelled.

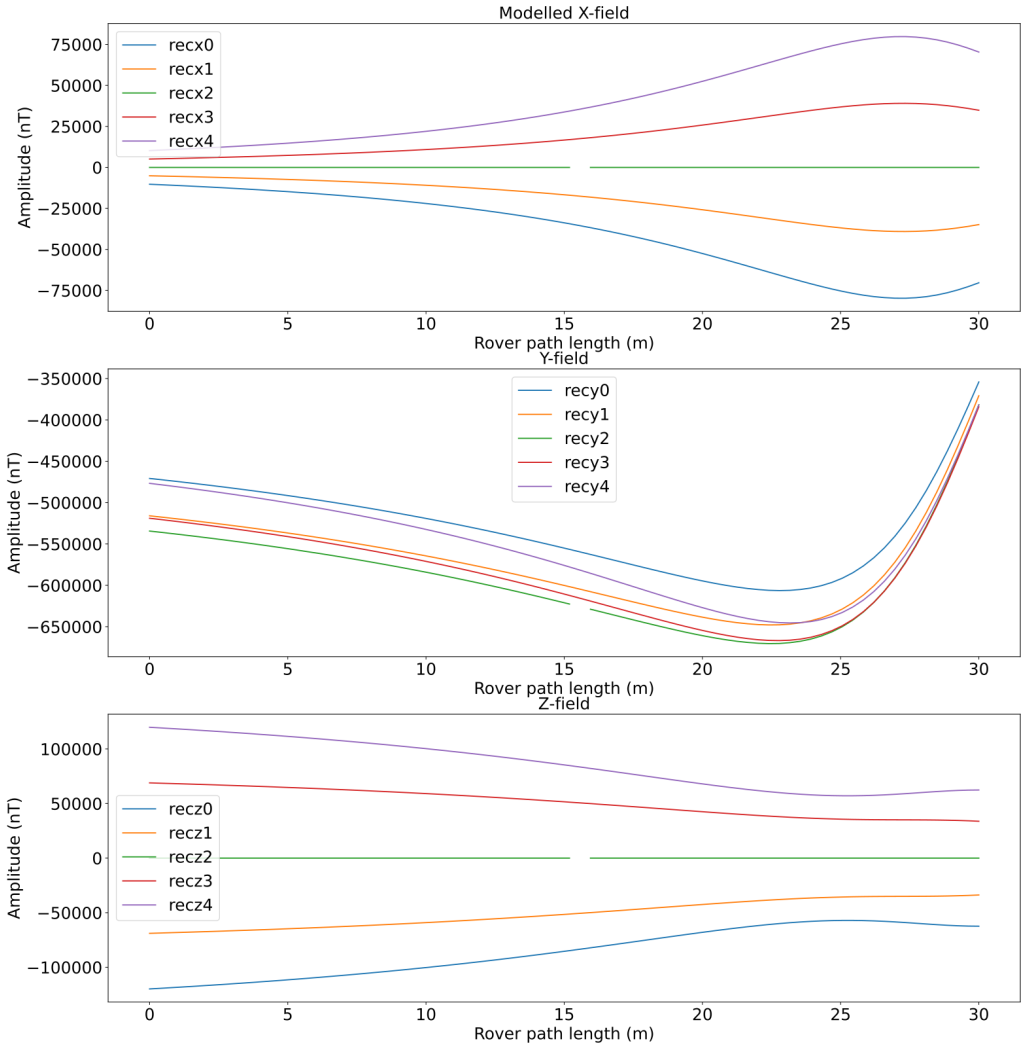

Figure 5-16: The magnetic x- y- and z-components for the substation busy zone area are presented as conceptualised in Figure 4-10.

Chapter 6

Discussion of results, conclusions and recommendations

6-1 Discussion of results

Some assumptions do not hold in the real world. The Earth is not one dimensional, for instance. Complex resistivity differences exist, such as wind turbine monopiles in 'busy zones', pipelines and other conductive underwater infrastructure. However, this report has given a baseline for describing offshore buried cables. Starting with the land measurements, the Empymod models and Biot-Savart's Law give a good approximation for the magnetic field of a cable with a known current and distance. The accuracy of those measurements are in the range of 2-15%. The two separate land measurements confirm this statement. Important to note is that un-shielded single phase cables were used in the land measurements. Submarine power transmission cables are shielded and have three cores, which are 120°out of phase to reduce losses. Furthermore, it is of great importance to know the receiver positions, too. For land measurements these positions can be easily checked using GPS measurements. However, underwater positioning is not as simple. When doing tests underwater, the receiver positioning has a bigger error range which should be taken into account. All considered, the Empymod models give a good starting point for discovering the effects on the magnetic field of varying environmental parameters. The attenuation results show that it is best to stay within the ultra-low frequency range of sub 2000 Hz to keep at least 50% of the signal strength. When measuring live wind turbine cables this benchmark is met by the fact that they all operate at 50 Hz. Damaged wind turbine cables can leak voltage, reducing the signal even more, making the signal even weaker than 50%. Moreover, when a wind turbine is out of operation, a signal need to be generated artificially in the cable. The frequency and current of this signal needs to be very well known to make accurate forward models for magnetic field predictions. After comparing the different analytical models, it seems that on land Biot-Savart holds very well on land. This is beneficial for forward modeling, since this is the least difficult and computationally expensive way of modeling the magnetic field of a cable. It must be remembered however that Biot-Savart's Law is static, and therefore solves for all

frequencies. When filtering for a specific frequency underwater, the signal will be reduced. If this signal is reduced in an almost scaled fashion, which it appears to do, Biot-Savart's $1/R$ dependency can be used. Both dipoles and bipoles in Empymod agree with each other, and with Biot-Savart's law. When accommodating for more complex geometries, dipoles need to be used. When producing complex geometries with dipoles, it is not possible to always give them the appropriate current direction. In Empymod dipoles produce a field in all directions radially outward. 36 combinations exist for electromagnetic source and receiver pairs, but they are only perpendicular to one another. Therefore, to generate data for complex geometries, electric dipole vectors should be created by appropriately scaling different source-receiver configurations. As an example, say a cable is modeled which lies at an angle of 45°angle in the xy-plane as a sequence of dipoles (Figure 6-1). Then, to acquire the components, the magnetic field should be scaled with $1/\sqrt{2}$ for the x and y components, which with the z-component together will produce the total field, which can be found with the Biot-Savart solution (when considering whole space of air).

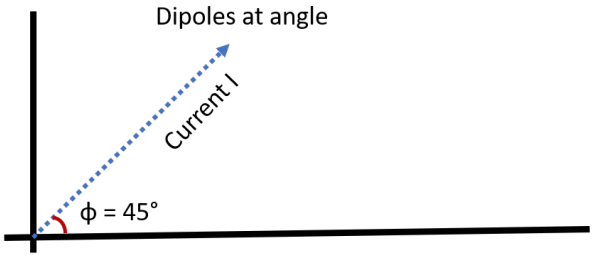

Figure 6-1: Dipoles at a 45°angle in the xy-plane.

Surrounding resistivity contrasts together with changes in water depth change the measured magnitude of the magnetic field by up to 10%, mainly in the y-component. However, different geometries and nearby cables have way larger effects. It is therefore of paramount importance to know the approximate location of your desired cable and nearby cables when surveying the magnetic field with fluxgate magnetometers. Furthermore, how you survey the cable: with the ROV at an angle, perpendicular or parallel to the cable, is vastly important. It is easiest to find the approximate cable position by surveying it perpendicular on a couple of lines, and then extrapolating its position. Peaks in the magnetic field will correspond to its position in the xy-plane, since the cable will be closest. Thereafter, if the signal changes a lot, it can be attributed to geometrical effects.

The Empymod package has several shortcomings. Firstly, the cable is assumed to be infinitesimally small, which they are not. Moreover, cable parameters such as three phase cables and cable shielding cannot be easily modeled. Offshore power cables also have lots of ground points with capacitors, which leak current. Therefore, if one does not know the current lost at which point the signal will change suddenly when surveying. How the magnetic field signal changes cannot be emulated in Empymod. Electromagnetic distortion is another big shortcoming in Empymod. Bleed over, bleed off, return currents and 3D geometry cannot be modeled in Empymod. Especially bleed over in areas where pipelines or cables are close to the cable you are tracking can cause signal losses. These losses can cause a signal loss of up to 60%, as investigated by ranging company Optimal-Ranging, 2012.

6-2 Conclusions

Conventional cable tracking methods like visual and acoustic surveying have troubles with finding buried offshore cables in particular. Electromagnetic methods circumvent a lot of these shortcomings because electromagnetic fields persist in the subsurface. This report gives an overview of the possibilities and shortcomings for offshore electromagnetic cable tracking, expands on the associated physics and expands on numerical modeling of offshore wind farm cables with example scenarios. Land measurements have shown that modeling the cable using Empymod can reproduce the measured results accurately. Underwater measurements, however, will have bigger errors and difficulties due to the complexity of underwater rover positioning, as well as complex reflection coefficients of the magnetic field. Ultra-low frequency ranges up to 2000 Hz contain up to 50% of the signal underwater. Measuring with lower frequencies like 50 Hz, the frequency of live wind turbine cables, is recommended. Several source types can be used to accommodate for different geometries. More complex geometries require individual dipoles. For straight cables, using bipoles is just as accurate, but faster in terms of computational speed. The Python package agrees with Biot-Savart's Law in whole-space. Different layers and water depths have effect on the TE and TM mode, meaning it is imperative to know the water depth accurately to pinpoint its effect when doing offshore surveying. Even though the package is created for CSEM modeling, it is possible, efficient and effective to model offshore buried windmill cables in terms of their electromagnetic response in Empymod. Behaviour of the magnetic field in different environments can be evaluated very precisely and accurately, without changing more than one or two parameters at once. Water depth and inhomogeneous layering can influence the measured signal by up to 10%. However, the geometry of the tracked cable has by far the biggest influence on the measured response, possibly completely altering the signal. Therefore, some information about the cable position and geometry is needed beforehand to properly track the cable using fluxgate magnetometers.

6-3 Recommendations

Further studies are recommended to implement more complexity in the cables. Submarine power transmission cables have three phases, which are 120°out of phase to reduce magnetic losses. This three-phase component might make the measured magnetic field weaker than predicted by Empymod infinitesimally thin single phase cables. Furthermore, submarine cables are shielded by lead or other metallic alloys [Gill et al., 2012]. These highly conductive materials can have a big influence on the measured signal. Since single phase land cables can be accurately modeled in Empymod on land, to assess the influence of cable shielding and the three-phase component, it is recommended to do measurements on a known live cable on land. For those measurements, the position, current and frequency should be known to assess the influence of the shielding and three-phase problem. Comparing the measured signal of a more complex cable on land to Empymod models might give an understanding of their effects. COMSOL is a program in which more complex cables can be modeled. The package can model three-phase cables, the effects of the sheets and armour, and so forth. Integration of COMSOL into Empymod might give a better understanding of more complex cables. Moreover, at long distances submarine power cables need to be grounded at specific intervals to prevent too high of a voltage build up [Pedersen and Aanerud, 1977]. The grounding means that at certain locations there are losses within the cable. Usually around 60 to 80% of the power land on the shore of offshore wind farms, depending on the distance and whether HVAC or DC transmission is used. When surveying near the grounding points, the measured magnetic field signal can suddenly reduce unexpectedly. Surveying over known ground points can give an idea of the changes they cause and how they can be modeled. Lastly, integration between the forward models and inversion is recommended to improve the inversion results. Forward models are easier to generate than doing field measurements, which can be used to improve the inversion algorithm. Furthermore, matching measurements to forward models can help confirm or debunk cable positioning found by the inversion as a quality check.

Appendix A

Reproducibility

The Empymod package is open source, and available for download on the Empymod website. The scripts for the various tested models are stored in Gitlab. The research was done in partnership with Seekable, for which a confidentiality statement was signed by author S. Mossel. Therefore, the Gitlab access should be requested through e-mail, either at sil.mossel@seekable.nl or tobias.stolz@seekable.nl. The Gitlab has a good overview and a "ReadMe" file of the managed scripts, data and other material.

Appendix B

Data management

Organisational context	Forward modeling for electromagnetic subsea cable tracking has been conducted for an Msc thesis at TU Delft, commissioned by Seekable, under supervision of Prof. E. Slob, Msc. M. Künzel and Msc. T. Stolz
Research overview	Forward modeling of a cable is done to better understand the magnetic field of a buried electric cable source so it can more accurately and effectively tracked when maintenance or inspection is required.
Data management roles	Modelled data can be reproduced using the aforementioned gitlab link. The measured data is in the hands of League Geophysics and Seekable.
Type of data produced	The land measurement data owned by Seekable was used to verify the models. Synthetic data of the models is used to better understand hypothetical offshore scenarios. Both datasets are contained in binary files.
Software choices	GitLab and Dropbox are used for storing the synthetic data & models and measured data respectively.
Amount of data	The synthetic data is 1.71MB and the measured data 4.64 GB. The total required disk space of all data and scripts is around 6-7 GB.
Sharing ownership	Seekable's data is confidential but can be acquired on request.
Documentation and metadata	Both the Msc GitLab and Seekable GitLab have a ReadMe file for organisational purposes.
Long term storage	Everything is contained and will remain in the GitLab libraries.

Bibliography

[Abramowitz and Stegun, 1972] Abramowitz, M. and Stegun, I. (1972). Handbook of mathematical functions, vol. 55 of appl. *Math. Ser. 10th edition National Bureau of Standards US Governement Printing Office Washington, DC*, page 375.

[Asif et al., 2006] Asif, M., Rizal, M., and Yahya, A. (2006). An active contour for underwater target tracking and navigation. In *Proceedings of the International Conference on Man-Machine Systems*, pages 1–6.

[Bilgili et al., 2011] Bilgili, M., Yasar, A., and Simsek, E. (2011). Offshore wind power development in europe and its comparison with onshore counterpart. *Renewable and Sustainable Energy Reviews*, 15(2):905–915.

[Castillo-Reyes, 2021] Castillo-Reyes, O. (2021). Parallel edge-based tool for geophysical electromagnetic modelling. https://petgem.bsc.es/index.html. Accessed 08/07/2022.

[Castillo-Reyes et al., 2016] Castillo-Reyes, O., Puente, J. d. l., and Cela, J. M. (2016). Three-dimensional csem modelling on unstructured tetrahedral meshes using edge finite elements. In *Latin American High Performance Computing Conference*, pages 247–256. Springer.

[Cockett et al., 2015] Cockett, R., Kang, S., Heagy, L. J., Pidlisecky, A., and Oldenburg, D. W. (2015). Simpeg: An open source framework for simulation and gradient based parameter estimation in geophysical applications. *Computers & Geosciences*.

[Constable and Srnka, 2007] Constable, S. and Srnka, L. J. (2007). An introduction to marine controlled-source electromagnetic methods for hydrocarbon exploration. *Geophysics*, 72(2):WA3–WA12.

[Cox, 1981] Cox, C. S. (1981). On the electrical conductivity of the oceanic lithosphere. *Physics of the Earth and Planetary Interiors*, 25(3):196–201.

[Dinn, 2012] Dinn, G. (2012). Field experience with a new sub-bottom investigation tool: Acoustic 3-d imaging of the sub-seabed. In *2012 Oceans*, pages 1–9. IEEE.

[Dvorak, 2017] Dvorak, P. (2017). The future of cable maintenance and repair in offshore wind farms. *Windpower Engineering and Development*.

[Eymard et al., 2010] Eymard, R., Gallouët, T., et al. (2010). Finite volume method. *Scholarpedia*, 5(6):9835.

[Ferguson et al., 2012] Ferguson, A., de Villiers, P., Fitzgerald, B., and Matthiesen, J. (2012). Benefits in moving the inter-array voltage from 33 kv to 66 kv ac for large offshore wind farms. In *EWEA 2012 Conference Proceedings, Copenhagen, Denmark*, pages 16–19.

[Garrido et al., 2003] Garrido, C., Otero, A. F., and Cidras, J. (2003). Low-frequency magnetic fields from electrical appliances and power lines. *IEEE Transactions on Power Delivery*, 18(4):1310–1319.

[Gill et al., 2012] Gill, A. B., Huang, Y., Spencer, J., and Gloyne-Philips, I. (2012). Electromagnetic fields emitted by high voltage alternating current offshore wind power cables and interactions with marine organisms. In *Electromagnetics in Current and Emerging Energy Power Systems Seminar. London, UK. COWRIE*.

[Gresty, 2019] Gresty, A. (2019). Depth of burial – galloper offshore wind farm. *Hydro International*.

[Halliday et al., 2013] Halliday, D., Resnick, R., and Walker, J. (2013). *Fundamentals of physics*. John Wiley & Sons.

[Haus and Melcher, 1989] Haus, H. A. and Melcher, J. R. (1989). *Electromagnetic fields and energy*, volume 107. Prentice Hall Englewood Cliffs.

[Heald and Marion, 2012] Heald, M. A. and Marion, J. B. (2012). *Classical electromagnetic radiation*. Courier Corporation.

[Huera-Huarte, 2013] Huera-Huarte, F. J. (2013). Deep water: the next step for offshore wind energy. *Brussels, Belgium: A report by the European Wind Energy Association*.

[Hunziker et al., 2015] Hunziker, J., Thorbecke, J., and Slob, E. (2015). The electromagnetic response in a layered vertical transverse isotropic medium: A new look at an old problem. *Geophysics*, 80(1):F1–F18.

[Hyman and Shashkov, 1999] Hyman, J. M. and Shashkov, M. (1999). Mimetic discretizations for maxwell's equations. *Journal of Computational Physics*, 151(2):881–909.

[Incore, 2019] Incore (2019). *Incore Cables Cables in the renewable energy industry*. Incore Cables B.V.

[Isaacs and Goroshin, 2010] Isaacs, J. C. and Goroshin, R. (2010). Automated cable tracking in sonar imagery. In *OCEANS 2010 MTS/IEEE SEATTLE*, pages 1–7. IEEE.

[JHU, 2011] JHU (2011). Better turbine spacing for large wind farms. *Science Daily, John Hopkins University*.

[Johnston, 2017] Johnston, I. (2017). Artificial north sea island: Danish, dutch and german firms launch bid to make 'science fiction' plan a reality. *Independent*.

[Key, 2009] Key, K. (2009). 1d inversion of multicomponent, multifrequency marine csem data: Methodology and synthetic studies for resolving thin resistive layers. *Geophysics*, 74(2):F9–F20.

[Kitzing et al., 2020] Kitzing, L., Jensen, M. K., Telsnig, T., and Lantz, E. (2020). Multifaceted drivers for onshore wind energy repowering and their implications for energy transition. *Nature Energy*, 5(12):1012–1021.

[Littlefield et al., 2019] Littlefield, R. H., Soenen, K., Packard, G., and Kaeli, J. (2019). Seafloor cable based navigation and monitoring with autonomous underwater vehicles. In *OCEANS 2019 MTS/IEEE SEATTLE*, pages 1–5. IEEE.

[Lubofsky, 2019] Lubofsky, E. (2019). A new way of "seeing" offshore wind power cables. In *Researchers test ocean robots to make subsea cable surveys faster and cheaper*. WHOI.

[MacAskill and Mitchell, 2013] MacAskill, A. and Mitchell, P. (2013). Offshore wind—an overview. *Wiley Interdisciplinary Reviews: Energy and Environment*, 2(4):374–383.

[Messe-Düsseldorf, 2018] Messe-Düsseldorf (2018). Technical article 11 - wire 2018: Cables for offshore wind turbines.

[Moebs et al., 2016] Moebs, W., Ling, S. J., and Sanny, J. (2016). *University Physics Volume 1*. Rice University.

[Moon et al., 2014] Moon, W.-S., Kim, J.-C., Jo, A., and Won, J.-N. (2014). Grid optimization for offshore wind farm layout and substation location. In *2014 IEEE Conference and Expo Transportation Electrification Asia-Pacific (ITEC Asia-Pacific)*, pages 1–6. IEEE.

[Nichols, 2009] Nichols, G. (2009). *Sedimentology and stratigraphy*. John Wiley & Sons.

[Oppenheim et al., 1997] Oppenheim, A. V., Willsky, A. S., Nawab, S. H., Hernández, G. M., et al. (1997). *Signals & systems*. Pearson Educación.

[Optimal-Ranging, 2012] Optimal-Ranging (2012). Accurate utility depth measurements using the spar 300, orion.

[Pedersen and Aanerud, 1977] Pedersen, J. R. and Aanerud, L. A. (1977). Submarine power cable grounding means and method. US Patent 4,001,489.

[PMI, 2016] PMI (2016). Damage to subsea cables a huge risk to offshore wind farms (pmi underwater cable solutions).

[Ricketti, 2015] Ricketti, B. (2015). *Magnetostatics and the biot-savart law*. Heriot Watt University, School of Engineering and Physical Sciences.

[Rochlitz, 2022] Rochlitz, R. (2022). custem documentation version 1.2. https://custem.readthedocs.io/en/latest/. Accessed 08/07/2022.

[Rochlitz et al., 2021] Rochlitz, R., Seidel, M., and Börner, R.-U. (2021). Evaluation of three approaches for simulating 3-d time-domain electromagnetic data. *Geophysical Journal International*, 227(3):1980–1995.

[Rochlitz et al., 2019] Rochlitz, R., Skibbe, N., and Günther, T. (2019). custem: Customizable finite-element simulation of complex controlled-source electromagnetic data. *Geophysics*, 84(2):F17–F33.

[SiemensGamesa, 2022] SiemensGamesa (2022). How it all comes together at sea: installing an offshore wind farm. https://www.youtube.com/watch?v=mDvS7tizetgab$_channel$ = *SiemensGamesa*.

[Singh et al., 2004] Singh, U., Das, R., and Hodlur, G. (2004). Significance of dar-zarrouk parameters in the exploration of quality affected coastal aquifer systems. *Environmental Geology*, 45(5):696–702.

[Slob, 2020] Slob, E. (2020). *Electromagnetic Exploration Methods*. IDEA-League MSc program Applied Geophysics.

[Stewart et al., 2020] Stewart, J., Clegg, D. K., and Watson, S. (2020). *Calculus: early transcendentals*. Cengage Learning.

[Stolz, 2019] Stolz, T. (2019). Inversion algorithm development for passive electromagnetic detection of line sources.

[Stratton, 2007] Stratton, J. A. (2007). *Electromagnetic theory*, volume 33. John Wiley & Sons.

[Streich and Becken, 2011] Streich, R. and Becken, M. (2011). Electromagnetic fields generated by finite-length wire sources: comparison with point dipole solutions. *Geophysical Prospecting*, 59(2):361–374.

[Szyrowski et al., 2015] Szyrowski, T., Sharma, S., Sutton, R., and Kennedy, G. (2015). Subsea cable tracking in an uncertain environment using particle filters. *Journal of Marine Engineering & Technology*, 14(1):19–31.

[Szyrowski et al., 2013] Szyrowski, T., Sharma, S. K., Sutton, R., and Kennedy, G. A. (2013). Developments in subsea power and telecommunication cables detection: Part 1-visual and hydroacoustic tracking. *Underwater Technology*, 31(3).

[Wei et al., 2021] Wei, S., Liao, X., Zhang, H., Pang, J., and Zhou, Y. (2021). Recent progress of fluxgate magnetic sensors: basic research and application. *Sensors*, 21(4):1500.

[Werthmüller, 2017] Werthmüller, D. (2017). Getting started with controlled-source electromagnetic 1d modeling. *The Leading Edge*, 36(4):352–355.

[Wertmüller, 2022] Wertmüller, D. (2022). Empymod user guide and documentation. https://empymod.emsig.xyz/en/stable/manual/about.html. Accessed 08/07/2022.

[Wirth et al., 2008] Wirth, S., Ortiz, A., Paulus, D., and Oliver, G. (2008). Using particle filters for autonomous underwater cable tracking. *IFAC Proceedings Volumes*, 41(1):161–166.

[Xiang et al., 2016] Xiang, X., Yu, C., Niu, Z., and Zhang, Q. (2016). Subsea cable tracking by autonomous underwater vehicle with magnetic sensing guidance. *Sensors*, 16(8):1335.